Scholars' Mine

Summer 2018

Numerical modeling of capillary-driven flow in open microchannels: An implication of optimized wicking fabric design

Mehrad Gholizadeh Ansari

NUMERICAL MODELING OF CAPILLARY-DRIVEN FLOW IN OPEN

MICROCHANNELS: AN IMPLICATION OF OPTIMIZED WICKING FABRIC

DESIGN

by

MEHRAD GHOLIZADEH ANSARI

A THESIS

Presented to the Faculty of the Graduate School of the

MISSOURI UNIVERSITY OF SCIENCE AND TECHNOLOGY

In Partial Fulfillment of the Requirements for the Degree

MASTER OF SCIENCE IN ENVIRONMENTAL ENGINEERING

2018

Approved by

Dr. Wen Deng, Advisor
Dr. Joseph Smith
Dr. Jianmin Wang
Dr. Xiong Zhang

PUBLICATION THESIS OPTION

This thesis has been formatted using the publication option:

Paper I, pages 16-52, are intended for submission to the Journal of Computational Physics.

ABSTRACT

The use of microfluidics to transfer fluids without applying any exterior energy source is a promising technology in different fields of science and engineering due to their compactness, simplicity and cost-effective design. In geotechnical engineering, to increase the soil's strength, hydrophilic wicking fibers as type of microfluidics have been employed to transport and drain water out of soil spontaneously by taking advantage of natural capillary force without using any pumps or other auxiliary devices. The objective of this study is to understand the scientific mechanisms of the capability for wicking fiber to drain both gravity and capillary water out of soil fills.

In this work, wicking fibers were numerically modeled as open microchannels. The effect of the geometry and wettability on the spontaneous flow were analyzed. A 3D computational fluid dynamics-based model was developed to predict the transient movement of the meniscus in microchannels of different geometries. The Volume-of-Fluid (VOF) method was employed along with an in-house developed algorithm to refine the grid only at the air-water interface to reduce the computational effort. Analytical and numerical criteria were derived to determine the critical contact angle for spontaneous flow in different geometry open microchannels. It was found that the aspect ratio and channel geometry have a significant effect on the water filling velocity and mass flowrate. The study was extended to water drainage from unsaturated soils and the minimum negative inlet pressure which represents the maximum soil suction was determined numerically for spontaneous flow for different microchannel geometry. Results of this study can provide an implication in the design of wicking fibers and other microfluidic systems.

ACKNOWLEDGMENTS

I would like to express my sincere gratitude to my advisor, Dr. Wen Deng, for his guidance, patience, and support. My special word of thanks goes to my committee members, Dr. Joseph Smith, Dr. Jianmin Wang and Dr. Xiong Zhang for their support of this research.

I express my heart-felt gratitude to Dr. Joseph Smith for granting me access to the STAR-CCM+ license servers. His constant guidance, cooperation, motivation and support have always kept me going ahead.

I owe my deepest gratitude towards my family, Farimah, Hamid and Mahta for their eternal support and understanding of my goals and aspirations. Their infallible love and support has always been my strength.

A special thanks to my friends, Kiyavash, Kiarash, Behrouz and Elieh and all the other Amoos for their love, motivation and affection.

TABLE OF CONTENTS

LIST OF FIGURES

LIST OF TABLES

NOMENCLATURE

Symbol	Description
$\hat{n}_w$	Unit vector normal to the wall
$\hat{t}_w$	Unit vector tangential to the wall
F_{SF}	Volumetric surface tension force at the interface
$\hat{n}$	Surface normal
μ_g	Gas Dynamic viscosity
μ_l	Liquid Dynamic viscosity
ρ_g	Gas Density
ρ_l	Liquid density
a	Time step adaption factor
Co	Courant Number
F	Liquid volume fraction
G	Gas
i	Phase
L	Characteristic length
L	Liquid
p	Pressure
S	Solid
T	Temperature
t	Time
V	Liquid volume

x	Meniscus location
Δt_{max}	Maximum time step size
Δt_{min}	Minimum time step size
Δx_c	Current grid size
Δx_d	Default grid size
Δt	Time step size
Δx	Grid size
$\Delta \rho$	Difference in the density of the two phases
A	Surface area
Bo	Bond number
G	Gibbs Free Energy
S	Entropy
d	Channel depth
dV	Change in the liquid volume
g	Gravitational acceleration
k	Mobility parameter
n	Normal vector
p	Channel width to depth ratio
t	Unit vector
u	Velocity
w	Channel width
α	Bottom corner angle in a V-shaped channel

γ	Surface tension
θ	Contact angle
κ	Mean curvature of the free surface
μ	Dynamic viscosity of the liquid-gas mixture
ρ	Density of the liquid-gas mixture

1. INTRODUCTION

1.1   APPLICATIONS

Microfluidics is defined as the study of fluid flow behavior in small geometries, typically sub-millimeter, scale. There is an increasing rise in the use of spontaneous capillary flow (SCF) to transport fluid in microchannels in many different technologies. In biochemical or biotechnological applications, biological or chemical targets are transported through the microchannels without the use of pumps or syringes. This method helps with the simplicity of the design and low-cost fabrication of the microchannels as well as making them user-friendly and compatible to telemedicine. Point Of Care Testing (POCT) is referred to those medical tests that can be done where the patient is, which allows the patients to monitor and adjust their own treatment without having to go to a hospital or a medical center[1][2]. A simple example for POCT can be described in blood collection devices shown in Figure 1.1. The tip of the finger is punctured and using a simple glass capillary tube, the blood flows inside the device due to the surface tension.
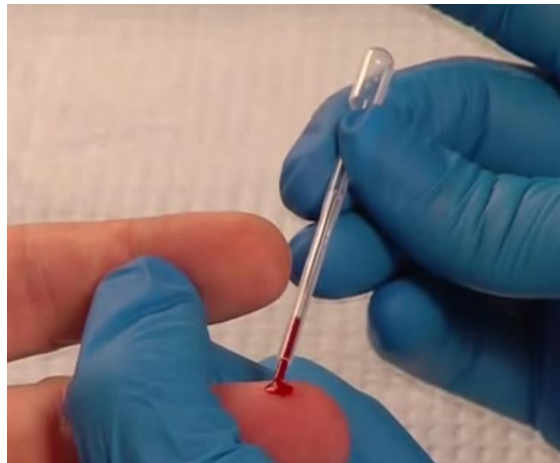
Figure 1.1. Blood collection device for Point Of Care Testing (POCT) [3].

The tube can be designed to collect an exact volume of blood depending on the medical test and the simple plastic bulb at the end of the tube is used to remove the collected blood sample.

There is a growing interest in the use of capillary tubes inside fuel cells to transport the chemical fuel internally[4]. Fuel cell is a device that converts chemical energy from a fuel into electricity through a chemical reaction. This fuel is usually injected into a reservoir and then it is transported into the internal cells where the chemical reaction occurs. Figure 1.2 shows the schematic design of self-pumping fuel cell where the fuel is transported spontaneously through the cell from reservoir 2. The chemicals react at the interval cells and the products of the reaction leave the cell through the capillary tubes from reservoir 3. In this design, the use of pumps or any other auxiliary devices has been avoided and the capillary action drives the reacting fuel in and outside the cell. Therefore, compared to the conventional fuel cells, the design becomes much smaller, simpler and more cost-effective.
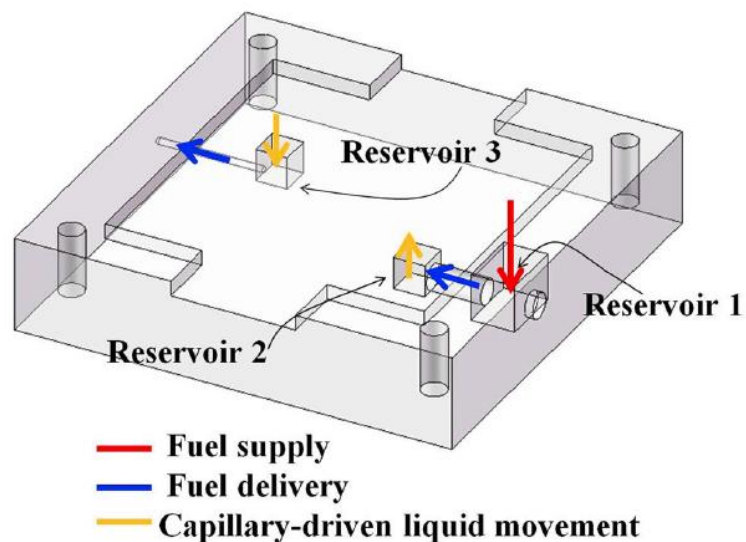
Figure 1.2. Schematic design of a self-pumping fuel cell[4].

Capillary tubes and wicks are also commonly used in the design of cooling systems and heat pipes[5][6]. Heat pipes are closed evaporator-condenser systems with a very high heat flux transport capability. The pipe consist of an evaporator section, a condenser section and an adiabatic section. Distilled water, liquid Ammonia, Sodium or Methanol is recycled as the working fluid from the condenser to the evaporator through a wick by the capillary action to transport energy. The continuous heat transfer process is represented in Figure 1.3. Heat is applied externally to the evaporator side and is conducted through the pipe wall where it vaporizes the working fluid. The resulting vapor pressure drives the vapor through the adiabatic section to the condenser where the vapor condenses and releases the latent heat of vaporization. The capillary pressure created by the menisci in the wick pumps the fluid back to the evaporator section. This process will continue as long as there is sufficient capillary pressure to drive the condensate back to the evaporator.
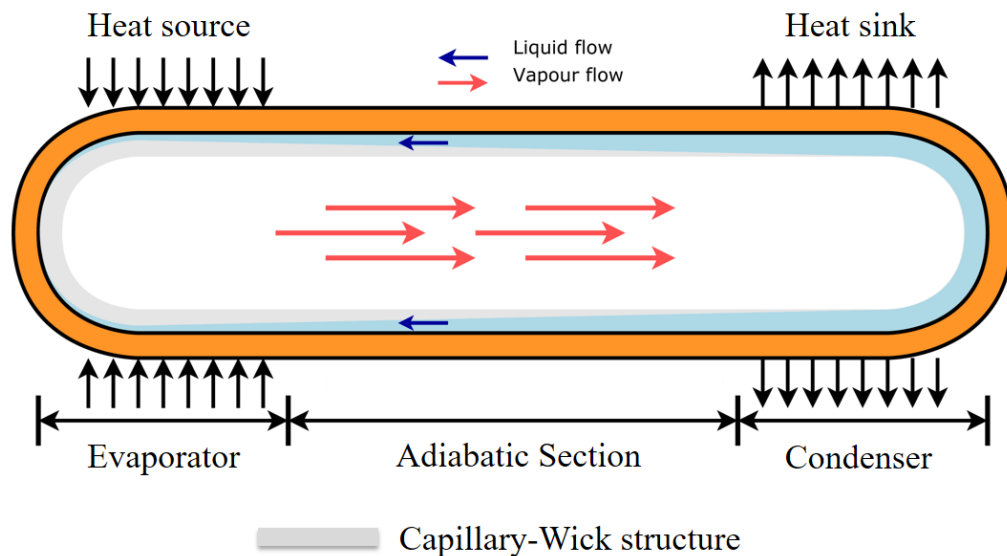
Figure 1.3. Mechanism of energy transfer in a heat pipe[7].

Capillary-driven flow is also widely used in space systems in the design of Propellant Management Devices (PMDs) to ensure gas free liquid delivery to the outlet of spacecraft propellant tanks [8][9]. In geotechnical engineering, capillary action can be used to drain and transport water from soil using wicking fibers [10]. The hydrophilic fibers shown in Figure 1.4 contain thousands of irregular shaped unconfined microchannels with a very high surface to volume ratio that allow the water to flow inside due to surface tension and capillary action.
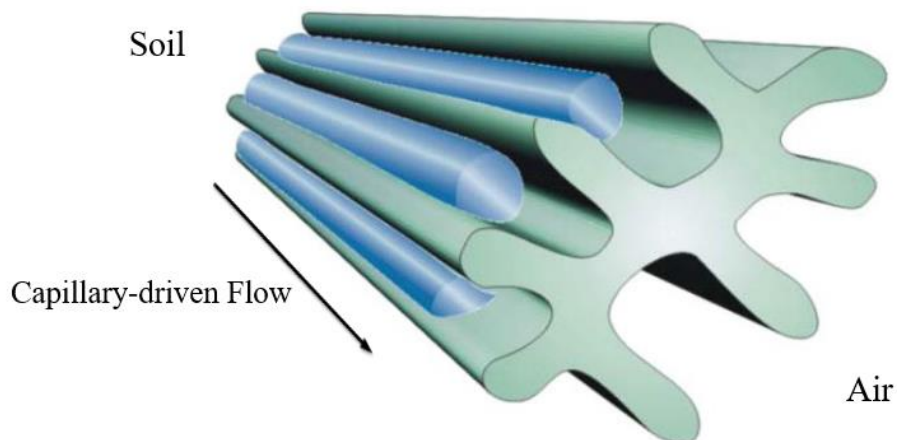
Figure 1.4. Hydrophilic wicking fibers removing water from soil[10].

The removal of water from the soil increases the soil's strength and stability. The application of the wicking fabric in water removal from soil is represented in Figure 1.5. Figure 1.5a shows a road with a very high soil water content. It's apparent that the soil is extremely soft as the wheel tracks can be readily seen on the road. Figure 1.5b shows how stiff the same soil has become after a one year treatment and draining water using the wicking fabric.
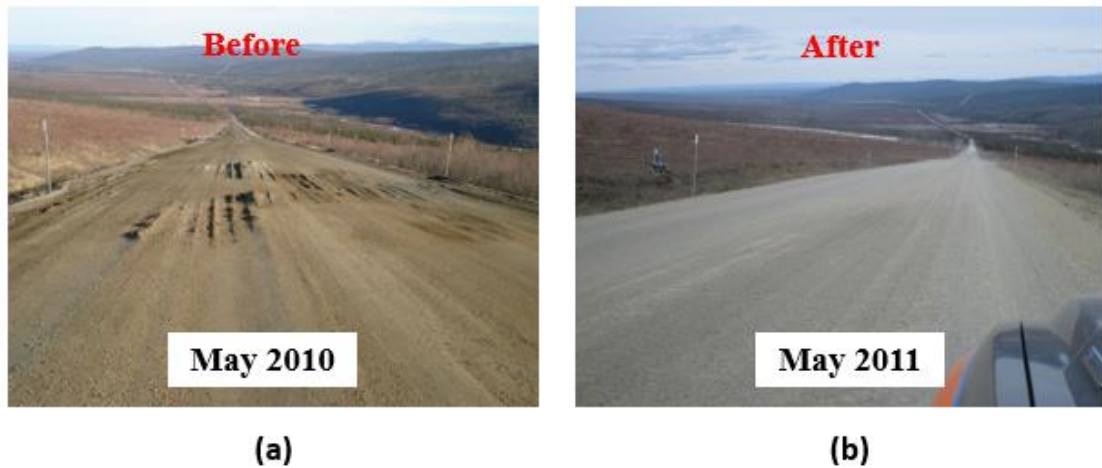
Figure 1.5. Wicking fabric application to drain water from a road embankment: (a) Before treatment with the wicking fabric, (b) after treatment with wicking fabric.

1.2   SURFACE TENSION

When a liquid droplet is deposited on a homogenous solid surface, two different equilibrium regimes are observed [11]: Partial wetting where the liquid drop has a finite contact angle θ with the surface and completely wetting where the liquid spreads on the solid surface as a thin molecular film (Figure 1.6).
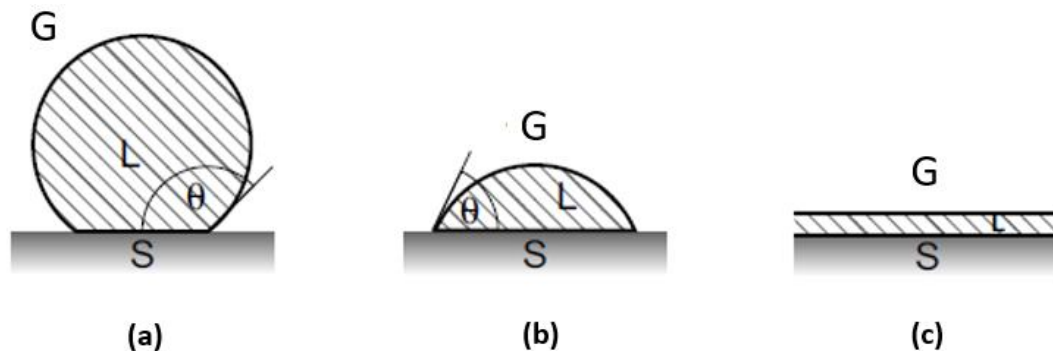
Figure 1.6. Shape equilibrium of a liquid droplet (L) on a solid surface (S), surrounded by the gas (G). (a) non-wettable, (b) and (c) wettable. (b) is partially wetted and (c) is completely wetted $\theta = 0$.

The free energy per unit area associated to each interface (solid, liquid and gas) are related using the contact angle θ through Young's equation [12].

$$\gamma_{LG} \cos(\theta) = \gamma_{SG} - \gamma_{SL} \tag{1}$$

where γ_{LG}, γ_{SG} and γ_{SG} represent the surface tensions associated with Liquid-Gas, Solid-Gas and Solid-Liquid interfaces. The surface is referred to as wettable if the liquid droplet has a contact angle of $\theta < 90°$ with the solid surface and non-wettable where $\theta > 90°$. In the two cases mentioned, if the working liquid is water, the surface is called hydrophilic and hydrophobic, respectively.

1.3 YOUNG-LAPLACE LAW

The surface tension at the liquid-gas interface causes a pressure difference across the curved interface (meniscus) which is also known as the capillary pressure. Young and Laplace developed a mathematical description of the mean curvature to predict this pressure difference as:

$$\Delta P = 2\gamma\kappa = \gamma\nabla.\hat{n} = \gamma \left(\frac{1}{R_1} + \frac{1}{R_2}\right) \tag{2}$$

where ΔP is the pressure difference is across the interface, γ is the surface tension, κ is the mean curvature of the free interface, $\hat{n}$ is the unit vector normal to the curvature interface and R_1 and R_2 are the principal radii of curvature at the interface (see Figure 1.7). In a capillary tube, the curved interface will produce a net force (negative pressure) in the direction of filling and the filling occurs spontaneously as long as the pressure at the inlet tube is smaller than the capillary pressure.
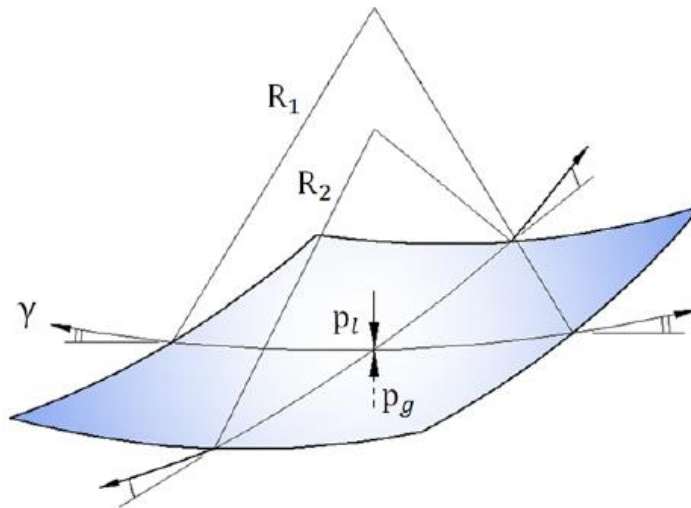
Figure 1.7. Schematic of the minimum and maximum principal osculating circle radius of the curvature at the interface [13].

1.4   DIMENSIONLESS NUMBERS

The dimensionless numbers are a set of dimensionless quantities that play an important role in modeling and predicting the fluid flow behavior. Through the modeling of a process, many assumptions may be considered for simplification purposes and the understanding the dimensionless numbers can help to determine whether the assumptions made are valid for the case of interest.

The importance of the body forces (gravity) compared to the surface tension force is determined by the Bond number (Bo):

$$Bo = \frac{\Delta \rho g L^2}{\gamma} \tag{3}$$

where $\Delta \rho$ is the difference in the density of the two phases, g is the gravitational acceleration, L is the characteristic length and γ is the surface tension. The Bond number is proportional to the squared of the characteristic length which makes it considerably small

in microfluidic systems. Therefore, the gravity gives a small contribution to the flow compared to the surface tension and it can be excluded from the analysis.

The next important dimensionless number is the Reynolds number (Re) which expresses the ratio between the inertial and viscous forces in the flow:

$$Re = \frac{\rho u L}{\mu} \tag{4}$$

where u is the average velocity inside the microchannel and μ is the dynamic viscosity. The relatively small Reynolds number in small scale flows, such as microfluidics makes the assumption of laminar flow valid. This can be considered as a disadvantage in terms of mass transfer rates, which makes the microfluidic devices bad mixers compared with large scale systems that operate at the turbulent flow regimes [14].

1.5   OBJECTIVES

It is essential to gain knowledge on fluid behavior in the capillary systems to ensure a design that allows spontaneous flow. Information on the maximum velocity and whether the channel can be filled with the liquid during the given time lapse and the conditions for spontaneous flow can be the key parameters for design and the choice of material in these systems.

The goals of this work are as follows:

- To develop a high-fidelity model to predict the multiphase behavior in open microchannels

- To develop analytical and numerical criteria for the spontaneous flow in microchannels of different shapes

- To analyze the effect of geometry on the liquid filling velocity in microchannels of different shapes

- To analyze the effect of negative inlet pressure on the spontaneous flow in microchannels of different shapes

2. METHODOLOGY

The study and analysis of capillary driven flow is very challenging and the little progress in this scientific area since the 1920s confirms this fact. First, these processes typically occur in small time scales and within the length scales of few millimeters. Therefore, the visualization of the flow dynamics through experiments may be hard or impossible without utilizing expensive laboratory equipment such as a high-speed camera. Moreover, the time and cost associated to manufacturing microfluidic devices for experimental purposes make the whole study more challenging. Secondly, the interactions between the phases at the interface and the change in the properties of the fluid such as viscosity and density can make the analytical modeling very challenging. Some assumptions can be made to simplify the governing equations and maybe in special cases, there is a possibility of deriving an analytical solution. Nevertheless, these assumptions and oversimplifications can completely change the physics and cause a divergence between the predictions of the derived analytical solution and the actual natural phenomena.

Thanks to the tremendous advancement of computational power over the past decades, numerical modeling of the multiphase flow has become a suitable remedy for the mentioned challenges. Using Computer-Assisted Design (CAD), real word experiments can be conducted virtually and still provide comprehensive information. This approach reduces the effort and time required for the experiment preparations and contributes to a more cost-effective design cycle. Nevertheless, the numerical modeling of transport phenomena has its own challenges. In our case of interest, for instance, the interface morphology is important as it determines the surface tension force that dominates the

pressure and flow field inside the droplet in capillary-driven flow. In the numerical modeling of the interaction between two immiscible fluids, a marker function is defined and updated in every time step based on the location of the interface. In the Eulerian multiphase modeling, the interface location is updated implicitly from the advected marker function. The examples of Eulerian models are Volume-of-Fluid (VOF)[15], Level-Set (LS)[16] and phase field method[17]. In general, Eulerian multiphase methods are good at capturing a sharp interface between the phases, especially in those cases that the interface goes through large deformations. Nevertheless, they suffer from the implicit interface reconstruction. The Volume-of-Fluid method, for instance, requires a local fine grid at the interface in order to predict a sharp and accurate orientation of the interface[18].

The objective of this study is to implement the suitable multiphase numerical method to predict the fluid behavior in capillary-driven flow and gain knowledge on its physics in various applications. The Volume-of-Fluid method is used to capture the sharp interface between the two immiscible fluids and two algorithms are developed to address the need of fine computational gird at the interface and to increase the numerical stability of the solver.

2.1   ADAPTIVE GRID REFINEMENT

One of the major drawbacks of the Volume-of-Fluid method is that the morphology of the gas-liquid interface is highly dependent on the resolution of the grid at that point. And in order to achieve a high quality and accurate predictions of the interface location, there is a significant need for local grid refinements. Over the past decade, the most common approach to address this issue was to implement a fixed grid and use localized

refinements in the computational grid where the high gradients of density or phase volume fraction are expected. While this method reduces the computational effort a lot compared to the conventional numerical studies where the whole gird was refined, there are still unnecessary refined regions in the grid that add up to the simulation run-time and make the model computationally more expensive.

Let us consider the two case studies represented in Figure 2.1. In both cases, the capillary-driven flow is studied in an open circular channel with a depth of 10 μm and lengths of 250 μm (a) and 500 μm (b). Fixed localized refinement has been implemented for case (a), whereas in case (b), the grid has been only refined at the gas-liquid interface using an adaptive algorithm. The minimum cell size for case (a) is 0.5 μm while it is 0.25 μm in case (b). Regardless of the fact that the channel in case (b) is twice longer than case (a) and the minimum mesh cell size in case (b) is two times smaller than the first case, there has been a significant save on the number of elements.

(a)   (b)
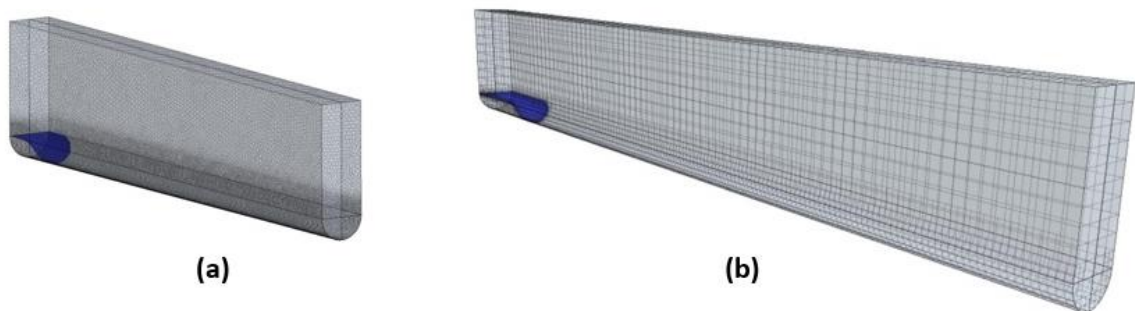
Figure 2.1. Computational grid in an open circular microchannel. (a) Fixed localized refinement at the bottom of the channel and (b) Adaptive refinement at the phases interface.

In terms of simulation run-time, it would take 12.7 days to run the simulation on 650k cells using 32 CPU cores for case (a), whereas the simulation for 11k cells of case (b)

takes 18.4 hours using only 2 CPU cores. Therefore, the adaptive algorithm helps reducing the computational effort drastically as well as providing results with a higher quality. This approach is extremely promising in terms of saving the simulation run-time, especially for the study of high length to depth ratio microchannels. The algorithm developed for the adaptive mesh refinement is represented in Figure 2.2. The solver starts to iterate for n number of time steps before refining the mesh, where n is user-defined. A volume fraction threshold of 8 percent is defined and for those cells that the volume fraction of water f is between 0.08 and 0.92, the mesh is refined and the other remaining cells are coarsened with the default cell size of Δx_d. To avoid over-refinement and have control over the number of cells, the minimum refined cell size is defined based on the maximum value between 0.1 μm and $\frac{\Delta x_c}{8}$, where Δx_c is the current cell size in each cell.
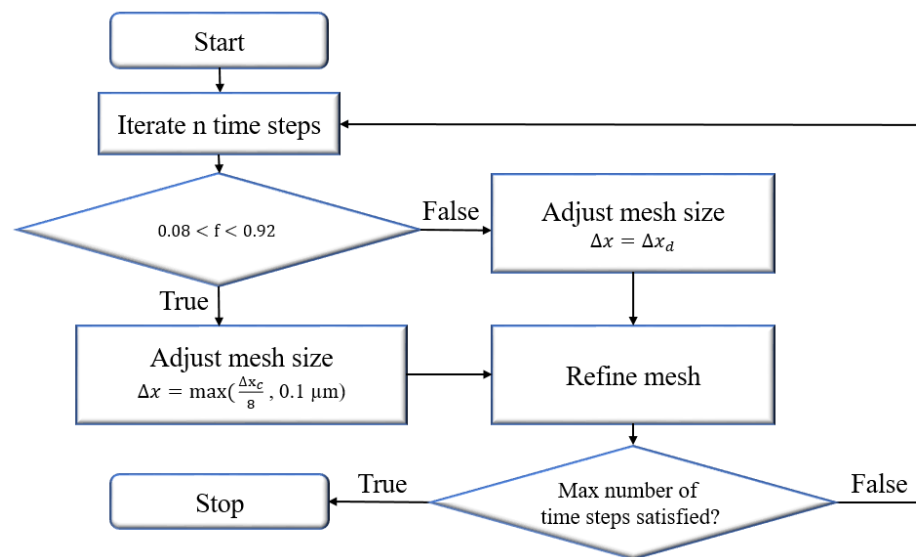
Figure 2.2. Adaptive grid refinement algorithm.

This algorithm is looped until the maximum number of time steps is satisfied.

2.2   ADAPTIVE TIME STEP

In order to ensure the stability of a transient numerical model, the time step has to be controlled. Most numerical models tend to diverge at the early time steps due to assignment of unrealistic initial/boundary conditions. To avoid divergence, it is generally recommended to use a small time step at the beginning of the run and increase the time step gradually when the numerics become more stable. The time step can be adapted based on the maximum fraction of the computation cell in which the fluid travels through in a single time step. This fraction as also known as the dimensionless Courant number:

$$Co = \frac{\Delta t}{\frac{\Delta x}{u}} \tag{5}$$

where Δt is the time-step, Δx is the grid size and u is the fluid velocity. In transient numerical analyses, it is generally recommended to set the maximum Courant number to 0.25 and adapt the time step based on this criteria[19][20]. An algorithm is developed through a JAVA Script code that is coupled with our solver STAR-CCM+ that changes the time step based on the Courant number criteria of 0.2. The time step varies between 10^{-8} and 10^{-6} seconds based on the maximum value of the courant number in the whole computational domain using the algorithm shown in Figure 2.3. To insure the numerical stability, the solver starts to iterate for 100 time steps with a small time step of $\Delta t_{min} = 10^{-8}$ seconds. The Courant number is calculated in each computational cell using Equation 5 and the maximum Co value (Co_{max}) is compared with the specified minimum value of 0.2 and maximum of 0.8.
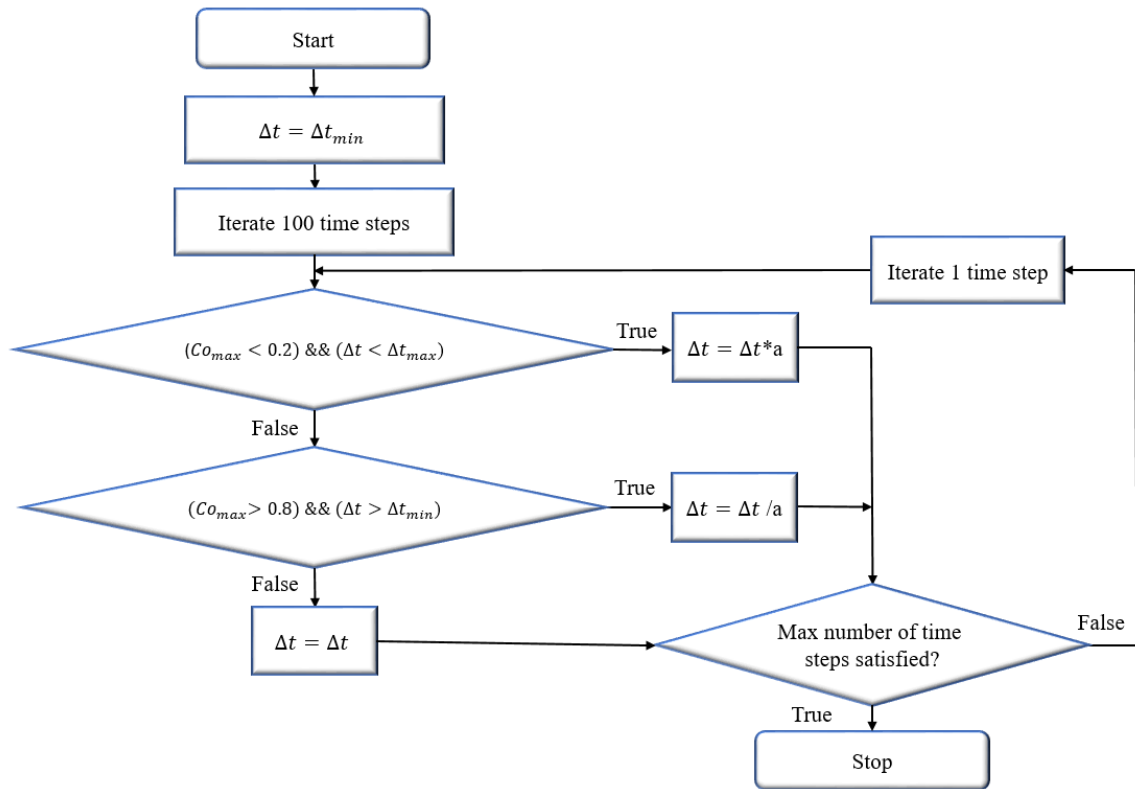
Figure 2.3. Adaptive time step algorithm based on the maximum Co number in the computational domain.

The current time step is multiplied or divided by the adaption factor a if the $Co_{max} < 0.2$ and $\Delta t < \Delta t_{max}$ or $Co_{max} > 0.8$ and $\Delta t > \Delta t_{min}$, respectively. In this current study $\Delta t_{max} = 10^{-5}$ and $\Delta t_{min} = 10^{-8}$ seconds and f is set to 1.10. This algorithm is looped until the maximum number of time steps is satisfied.

PAPER

I. NUMERICAL MODELING OF CAPILLARY-DRIVEN FLOW IN OPEN MICROCHANNELS

ABSTRACT

The use of microfluidics to transfer fluids without applying any exterior energy source is a promising technology in different fields of science and engineering due to their compactness, simplicity and cost-effective design. In geotechnical engineering, to increase the soil's strength, hydrophilic wicking fibers as type of microfluidics have been employed to transport and drain water out of soil spontaneously by taking advantage of natural capillary force without using any pumps or other auxiliary devices.

In this work, wicking fibers were numerically modeled as open microchannels and the effect of the geometry and wettability on the spontaneous flow were analyzed. A 3D computational fluid dynamics-based model was developed and validated to predict the transient movement of the meniscus in microchannels of different geometries. The Volume-of-Fluid (VOF) method was employed along with an in-house developed algorithm to refine the grid only at the air-water interface to reduce the computational effort. Analytical and numerical criteria, based on the second law of thermodynamics and the minimization of the Gibbs Free Energy were derived to determine the critical contact angle for spontaneous flow in different geometry open microchannels. The study was extended to water drainage from unsaturated soils and the minimum negative inlet pressure which represents the maximum soil suction was determined numerically for spontaneous

flow for different microchannel geometry. Results of this study can provide an implication in the design of wicking fibers and other microfluidic systems.

1. INTRODUCTION

1.1 MOTIVATION

Microfluidics is defined as the study of fluid flow behavior in small geometries, typically sub-millimeter, scale. There is an increasing rise in the use of spontaneous capillary flow (SCF) to transport fluid in microchannels in many different technologies [1][2]. In biochemical or biotechnological applications, biological or chemical targets are transported through the microchannels without the use of pumps or syringes. This method helps with the simplicity of the design and low-cost fabrication of the microchannels as well as making them user-friendly and compatible to telemedicine [3][4][5]. Capillary-driven flow is also widely used in space systems in the design of Propellant Management Devices (PMDs) to ensure gas free liquid delivery to the outlet of spacecraft propellant tanks[6]. In geotechnical engineering, hydrophilic wicks can be used to drain and transport water from soil using wicking fibers [7]. It is essential to gain knowledge on fluid behavior in these capillary systems. Information on the maximum velocity, whether the channel can be filled with the liquid during a given time lapse and the choice of material for the microchannels to ensure spontaneous flow can be the key parameters in designing these systems.

1.2 BACKGROUND

Capillary-driven flow has been studied as early as 1920. Nevertheless, the research progress in this area has been very slow due to constraints in experimental facilities and

the limitations of microchannel fabrication methods. Lucas and Washburn were the first to describe the dynamics of the flow in confined cylindrical microchannels. Neglecting the gravity and considering a balance between the capillary force and the viscous drag, they derived an implicit solution that showed the meniscus location increases proportional to the square root of time [8][9]. Inertia is ignored in the Lucas-Washburn model, assuming that flow is continuous under constant viscous laminar Poiseuille flow conditions. Bosanquet provided an improved modification of Lucas-Washburn theory and took account of fluid inertia and the acceleration occurring at the start of the flow in confined microchannels [10]. Many researchers developed their studies on both confined and open microchannels of arbitrary geometry based on the models of Lucas-Washburn and Busanquet. Tchikanda et al. provided an analytical approximation for predicting the mean velocity of fluid in an open rectangular microchannel for meniscus constant angles ranging from 0 to 90°[11]. Ichikawa's group studied the gas-liquid interface behavior in confined rectangular microchannels and obtained a dimensionless driving force for glass-water, glass-ethanol and ethanol-PDMS, by which the interface motion can be predicted for any size of rectangular microchannel[12]. Yang at al. proposed a one-dimensional analytical model that predicts the meniscus location and velocity with respect to time. They validated the square-root dependence through experimental work by fabricating Parylene and Silicon-nitride microchannels. They showed that the gravitational force may be generally neglected given the fact that they are orders of magnitude smaller than capillary force in hydrophilic microchannels. However, gravitational pumping may still push the capillary meniscus forward even encountering a hydrophobic dragging from the surface tension effect[13]. Chen et al. studied capillary rise flow in surfaces with different wicking

structures. They showed that the effect of porosity and geometry on the advancing rate of the meniscus is insignificant in open V-shaped and U-shaped channels, nevertheless, for the skewed channels, the closer the profile is to a straight channel, the greater is the advancing rate[14]. Mitra and Saha studied the effect of dynamic contact angle on meniscus profile in confined microfluidic channels with integrated pillars numerically and experimentally. Their study showed that the use of dynamic contact angle does not have a significant effect on the meniscus prediction and the use of static contact angle is adequate when using free surface Volume Of Fluid (VOF) algorithm for microfluidic applications[15].

Zhu and Petkovic observed that the dynamic contact angles in microchannels were significantly larger than those measured from a flat substrate and the angle varied with the channel size[16]. Kuo investigated the capillary filling speed of water inside confined nanochannels experimentally and numerically. Their experimental results and numerical results for the filling velocity agreed well and are somewhat smaller compared to the theoretical results due to the assumption of constant contact angle. Their study showed that the filling velocity decreases with the decrease of channel depth and increases with the increase of filling length and is independent of the channel width[17]. Cito et al. did a 2-D numerical analysis of the wall mass transfer rates of a first-order chemical reaction in confined rectangular and circular microchannels. They reported the effects of Reynolds number, contact angle and channel geometry on the time and the evolution of the local and averaged wall mass transfer rates[18]. Ouali et al. proposed a model for predicting the capillary rise in closed and open rectangular microchannels assuming Cassie-Baxter states and derived a dimensionless cross-over time below which the solution can be approximated

using the Bousanquet equation and above which by visco-gravitational solution[19]. Furrer's group conducted a series of experiments to visualize the behavior of liquid flow in a rectangular open channel (mm scale) and studied the liquid pressure drop due to viscous effects[20].

Yang et al. provided a modified Washburn equation that predicts the location of the meniscus inside open non-cylindrical microchannels. They also studied the dynamics of the capillary-driven flow for water and water-glycerol mixtures and proposed that for the channels of the same depth, higher liquid flow rates are achieved with the decreasing channel width, irrespective of the channel cross-section (rectangular or curved)[21]. Berthier et al. derived a general condition to predict the occurrence of spontaneous capillary flow (SCF) in confined and open microchannels with uniform cross-sections based on the assumption that the free gas-liquid interface evolves so that the Gibbs free energy is minimized. They suggest that for SCF, the generalized Cassie angle must be smaller than $90°$. The result is much simpler and straightforward for confined microchannels as the capillary line is the product of the surface tension by the cosine of the constant contact angle[22]. They generalized the Lucas-Washburn model which is only valid for cylindrical channels to determine the location and the velocity of the meniscus for the spontaneous capillary flow in confined microchannels of arbitrary shapes. They also showed that there is no change in the dynamic contact angle as the velocity decreases during capillary flow and in fact for intertialess flow with small Capillary and Reynolds number, the dynamic contact angle in nearly equal to the static contact angle[23]. They also investigated capillary velocities in closed channels and U-grooves[24]. Berthier's group extended their study to curved channels as well. They showed that the flow is

symmetrical along the midline at the curves inside suspended channels, but for open channels the flow becomes axisymmetric for contact angles smaller than $60°$. They also mention that contact angles are affected by the dynamic effects in the first lengths of the microchannel (up to approximately 20-40 hydraulic diameter) and then the contact angle becomes close to the static value[25]. In a later work, they extended their general condition for the establishment of spontaneous capillary flow (SCF) for channels of non-uniform cross-section. They reported that the flow does not flow indefinitely inside the diverging microchannel and stops at some location[26].

Yu's group established an one-dimensional theoretical model to determine flow rate limitations in an asymmetry open capillary channels and investigated the critical flowrates at which the surface collapses as a function of channel geometry and liquid properties[6]. Leon's group derived semi-analytical model which describes the flow in vertical open rectangular microchannels of different aspect ratios. As reported in other literature, for values of width/height higher than 2, their model does not provide a good estimation of the flow compared to the experimental results[27]. Sowers et al. performed flow measurements of liquid polydimethylsiloxane in open rectangular microchannels and validated their experimental results based on the analytical model provided by Yang et al. They assumed a free slip boundary condition at the gas-liquid interface and no-slip at the walls. They showed that the ideal width to depth ratio of microchannels is around 2 for achieving higher flow rates[28]. Lade's group studied capillary flow dynamics inside 3D printed open microchannels as a function of printing technology, print orientation, channel dimension and liquid properties. They provided guidelines for 3D printing microchannels as well as strategies for approaching potential printing problems[29].

In the mentioned numerical microfluidic studies, a rather coarse grid was employed to reduce the number of computational cells and provide faster results at the expense of low grid resolution at the gas-liquid interface. Nevertheless, the applicability of the popular Volume-of-Fluid (VOF) method that is used for free surface flow modeling highly depends on the computational grid. In other words, the gas-liquid interface shape and position depend on the mesh cell size and using an overall coarse mesh can result a false prediction for the meniscus location. In this work, this issue has been resolved by employing a mesh that regenerates itself based on the location of the moving interface. Moreover, different geometries are generated through Computer-Assisted design (CAD) which have never been evaluated before in the available microfluidic studies.

1.3   SPONTANEOUS CAPILLARY-DRIVEN FLOW

Spontaneous Capillary Flow (SCF) happens when capillary forces are the only driving force that cause the liquid flow and no auxiliary devices such as pumps or syringes are used. This independence of exterior energy source makes the design of microfluidic devices much more portable, cost-effective and simpler. In this chapter, we will demonstrate on the theoretical condition in which Spontaneous Capillary Flow occurs. According to the second law of thermodynamics, for any system reacting at the standard pressure and temperature (STP), the system generally evolves to achieve the minimum of the Gibbs free energy. If we consider a liquid droplet surrounded by air, the equilibrium position of the gas-liquid interface will generally form so that Gibbs Free Energy is minimized which is equivalent to minimization of the liquid surface area. Consider Gibbs Thermodynamic equation [30]:

$$dG = \sum_i \gamma_i \, dA_i - pdV - SdT \tag{1}$$

where T is the temperature, S is the entropy, V is the liquid Volume, p is the pressure at the liquid phase, γ_i is the liquid interface tension with different boundaries, A_i is the liquid contact areas with different boundaries and G is the Gibbs free energy. We consider a general case where the liquid volume is not constant ($dV \neq 0$) and assuming no heating in the system, the temperature becomes constant and the last term vanishes in Equation 1. The system evolves in the state of lower energy, thus:

$$\sum_i \gamma_i \, dA_i - pdV < 0 \tag{2}$$

We consider an open channel with a uniform cross-section. The liquid (L) is in contact with the Gas (G) and liquid (S) and the surface area between the L-G, S-G and S-L are named A_{LG}, A_{SG} and A_{SL}, respectively. The inlet is usually considered to be at the atmospheric pressure if we assume the reservoir of the fluid is sufficiently large ($p \simeq 0$). The liquid will flow inside the channel spontaneously as long as the pressure at the front gas-liquid interface is smaller than the inlet pressure. Thus, Equation 2 can be re-written as:

$$\sum_i \gamma_i \frac{dA_i}{dV} < 0 \tag{3}$$

If we consider Young's equation (Equation 4) for a liquid droplet, we can relate the surface tension between the liquid-gas (LG) to the surface tension of the solid-liquid (SL) and solid-gas (SG) based on Young contact angle (θ) (Figure 1):

$$\gamma_{LG} \cos(\theta) = \gamma_{SG} - \gamma_{SL} \tag{4}$$
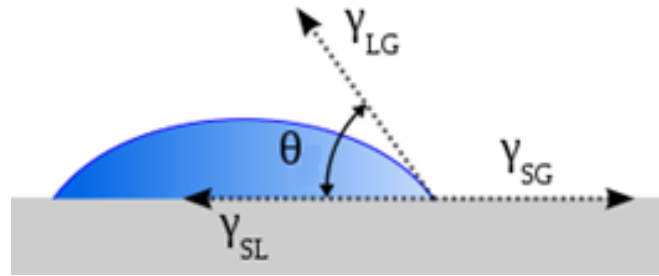
Figure 1. Contact angle of a liquid droplet wetted to a rigid solid surface.

If we consider all three phases, Equation 3 can be written as:

$$\sum_i \gamma_i \frac{dA_i}{dV} = \gamma_{SG} \frac{dA_{SG}}{dV} + \gamma_{SL} \frac{dA_{SL}}{dV} + \gamma_{LG} \frac{dA_{LG}}{dV} < 0 \qquad (5)$$

Note that any change in the surface area between the solid-liquid is made at the expense of the change is the surface area between the solid-gas ($dA_{SG} = -dA_{SL}$). Considering Equation 4, Equation 5 can be simplified to:

$$\frac{dA_{LG}}{dA_{SL}} < \cos(\theta) \qquad (6)$$

Equation 6 is a general condition for the Spontaneous Capillary Flow and it can be modified for different channel geometries. The morphology of the gas-liquid interface has been simplified in this approach, but it has been verified that this simplification does not affect the corresponding results significantly[22].

Let us consider an open rectangular channel and derive the SCF condition. Figure 2 shows the surface areas between the phases in the channel with the depth of d and width of w. dx is the infinitesimal change is the front location of the gas-liquid interface and dV is the change in the volume of the liquid.
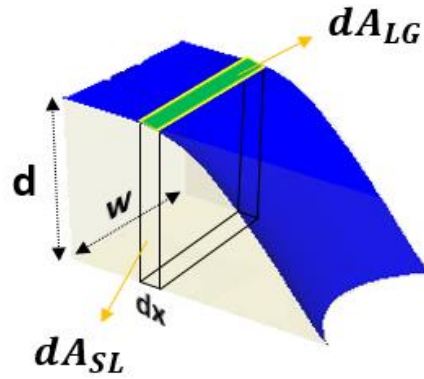
Figure 2. Contact areas between the phases in an open channel.

Based on Figure 2, we can write the changes in the surface areas as:

$$dA_{SL} = 2d \, dx + w \, dx \tag{7}$$

$$dA_{LG} = w \, dx \tag{8}$$

Using Equations 7 and 8, the condition 6 can be rewritten as:
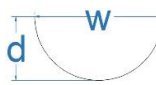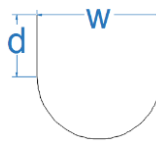
$$\frac{dA_{LG}}{dA_{SL}} = \frac{w \, dx}{2d \, dx + w \, dx} < \cos(\theta) \tag{9}$$

If we consider $(p = \frac{w}{d})$ and cancel out "dx", we have:

$$\frac{p}{2+p} < \cos(\theta) \tag{10}$$

Condition 10 shows that Spontaneous Capillary Flow occurs inside an open rectangular channel as long as the Young contact angle is smaller than $Arccos(\frac{p}{2+p})$, where p only depends on the aspect ratio of the channel. The same methodology can be used to determine the SCF criteria in channels for different geometries (Table 1). For instance, as long as the contact angle is smaller than $Arccos\left(\frac{2}{\pi}\right) = 50.46°$, liquid can spontaneously flow inside of an open circular microchannel.

Table 1. SCF criteria for different open microchannel geometries.

Channel Type	Geometry	SCF Criteria
Rectangular		$p = \dfrac{w}{d}, \qquad \theta < Arccos(\dfrac{p}{2+p})$
Circular		$\theta < Arccos(\dfrac{2}{\pi})$
U-shaped		$p = \dfrac{w}{d}, \qquad \theta < Arccos(\dfrac{2p}{4+\pi p})$
V-shaped		$\theta < \dfrac{\pi}{2} - \alpha$

2. NUMERICAL ANALYSIS OF CAPILLARY-DRIVEN FLOW

2.1 GOVERNING EQUATIONS

We assume that the fluid has a continue state of matter and describe the flow behavior using Navier-Stokes equations which are obtained from the conservation of mass, momentum and energy[31]. The system is considered to be isothermal and consist of two incompressible and immiscible fluids, which are represented as gas and liquid phase. Given the low Reynolds number, inertia is neglected and the flow is considered to be laminar and viscous forces are dominant. The Volume-of- Fluid (VOF) method is used to capture a sharp interface between the two phases in free surface flow modeling. This popular method was developed by Hirt and Nicholas[32] and it has a reasonable accuracy and more importantly it is computationally less expensive compared to the other Eulerian multiphase

models. Based on the assumptions made, the continuity and Navier-Stokes equations can

be written as:

$$\nabla . u = 0 \tag{11}$$

$$\frac{\partial \rho u}{\partial t} + \nabla . (\rho uu) = -\nabla P + \rho g + \nabla . \left(\mu (\nabla u + \nabla^T u) \right) + F_{SF} \tag{12}$$

where u is the mixture velocity, F_{SF} the volumetric surface tension force at the interface, t

the time, P the pressure and µ and ρ are the dynamic viscosity and density of the liquid-

gas mixture, respectively. The pressure force, shear force, gravitational force and surface

tension force F_{SF} balance the accumulation and convective momentum terms in the system

in Equation 12. The liquid volume fraction F is defined as the ratio of the cell volume

occupied by the liquid to the total volume of the corresponding cell. Where F = 1 shows

computational cells completely filled with liquid, F = 0 shows cells completely filled with

gas and 0 < F < 1 accounts for the gas-liquid interface. F is determined by solving the

continuity equation based on the assumption of incompressibility (Equation 13):

$$\frac{\partial F}{\partial t} + u . \nabla F = 0 \tag{13}$$

The mixture properties are calculated as weighted averages based on the volume fraction

function (Equations 14 and 15) where subscripts l and g represent the liquid and gas phases,

respectively:

$$\rho = F\rho_l + (1 - F)\rho_g \tag{14}$$

$$\mu = F\mu_l + (1 - F)\mu_g \tag{15}$$

The surface tension force is modeled as a volumetric force using Continuum Surface Force

(CSF) method proposed by Brackbill[33]:

$$F_{SF} = \gamma \kappa n + \frac{\partial \gamma}{\partial t} t \tag{16}$$

where γ is the surface tension and t is the unit vector in the tangential direction to the free surface and $n = \nabla F$ is the normal vector. Note that the surface tension coefficient is considered to be constant due to isothermal flow, therefore, the tangential force is zero and the second term in Equation 16 vanishes. κ is the mean curvature of the free surface, given as:

$$\kappa = -\nabla.\frac{n}{|n|} \tag{17}$$

If θ is the contact angle at the wall, then the surface normal at the cell next to the wall can be defined as:

$$\hat{n} = \hat{n}_w \cos(\theta) + \hat{t}_w \sin(\theta) \tag{18}$$

where $\hat{n}_w$ and $\hat{t}_w$ are the unit vector normal and tangential to the wall. The local curvature of the surface is calculated based on the contact angle and the surface normal and it is used to adjust the body force term F_{SF}.

The ratio of inertia to viscous force is determined by the dimensionless Reynolds number as:
$$Re = \frac{\rho u L}{\mu} \tag{19}$$

The dimensionless Bond number determines the importance of gravitational forces to surface tension forces is defined as:

$$Bo = \frac{\Delta \rho g L^2}{\gamma} \tag{20}$$

where $\Delta \rho$ is the difference in the density of the two phases, g is the gravitational acceleration, u is the average velocity inside the microchannel, L is the characteristic length, γ is the surface tension and μ is the dynamic viscosity. The characteristic length or the hydraulic diameter can be determined as follows:

$$L = \frac{4A_c}{P_w} \tag{21}$$

where A_c is the cross-sectional area of the channel and P_w is the wetted perimeter. The wetted perimeter of the channel is the total perimeter of all channel walls that are in contact with the flow.

The physical properties of the bulk liquid, gas phase and the surface property are shown in Table 2. Given that values for Bond number is much less than unity in microfluidic studies and in our present study, it is reasonable to neglect the gravitational forces compared to the surface force and the low Reynolds number confirms that our assumption for the laminar flow is valid.

Table 2. Fluid physical properties and surface characteristics.

Parameter	Unit	Water	Air
Density	$\frac{kg}{m^3}$	997.56	1.184
Dynamic viscosity	$\frac{kg}{m.s}$	8.88×10^{-4}	1.855×10^{-5}
Surface tension	$\frac{N}{m}$	0.074	-
Reynolds number ($\frac{\rho u L}{\mu}$)	-	~50	-
Bond number ($\frac{\Delta \rho g L^2}{\gamma}$)	-	$\sim8\times10^{-4}$	-

2.2   DIFFERENCING SCHEMES

The Equations 11 to 18 are solved numerically using the finite volume method (FVM), employed in the commercial CFD solver STAR-CCM+. The first-order upwind

has been used for momentum discretization. The Semi-Implicit Pressure Linked Equations (SIMPLE) algorithm is used to solve the equations sequentially and take care of pressure-velocity coupling as well as the non-linearity of the equations[34]. In order to avoid numerical diffusion at the interface and mimic the convective transport of immiscible components, the High Resolution Interface Capturing (HRIC) scheme is used for tracking sharp interface[35]. An adaptive time step is employed based on the Courant number criteria. The Courant number shows the fraction of a cell that the fluid travels through in a single time step:

$$Co = \frac{\Delta t}{\frac{\Delta x}{u}} \qquad (22)$$

where Δt is the time-step, Δx is the grid size and u is the fluid velocity. In order to increase the numerical stability of the solver, the *Co* was set to 0.2 and the time-step varied between 10^{-8} and 10^{-6} seconds based on the maximum value of the courant number in the whole computational domain.

One of the drawbacks of the VOF method is that it requires an ultra-fine mesh in order to predict a sharp interface between the phases. The microchannels modeled in the present study are about 10-80 μm wide and 1.5 mm long. A general coarse hexahedral mesh was defined and by coupling an in-house developed code with the solver, the grid was refined only at the phases interface.

Figure 3 represents the grid refinement in a U-shaped channel for three time values of 0.2, 0.75 and 1.5 ms. The 3D view of the water air interface is represented in Figure 3a. As it is observed, a very coarse mesh was defined in the computational domain and the mesh refinement moves along the channel with advancing meniscus. A 2D representation

of the grid refinement is shown in Figure 3b. A very sharp interface between the air and the liquid is resolved using the adaptive grid refinement and the transition between the phases occurs in only 2-3 refined computational cells.
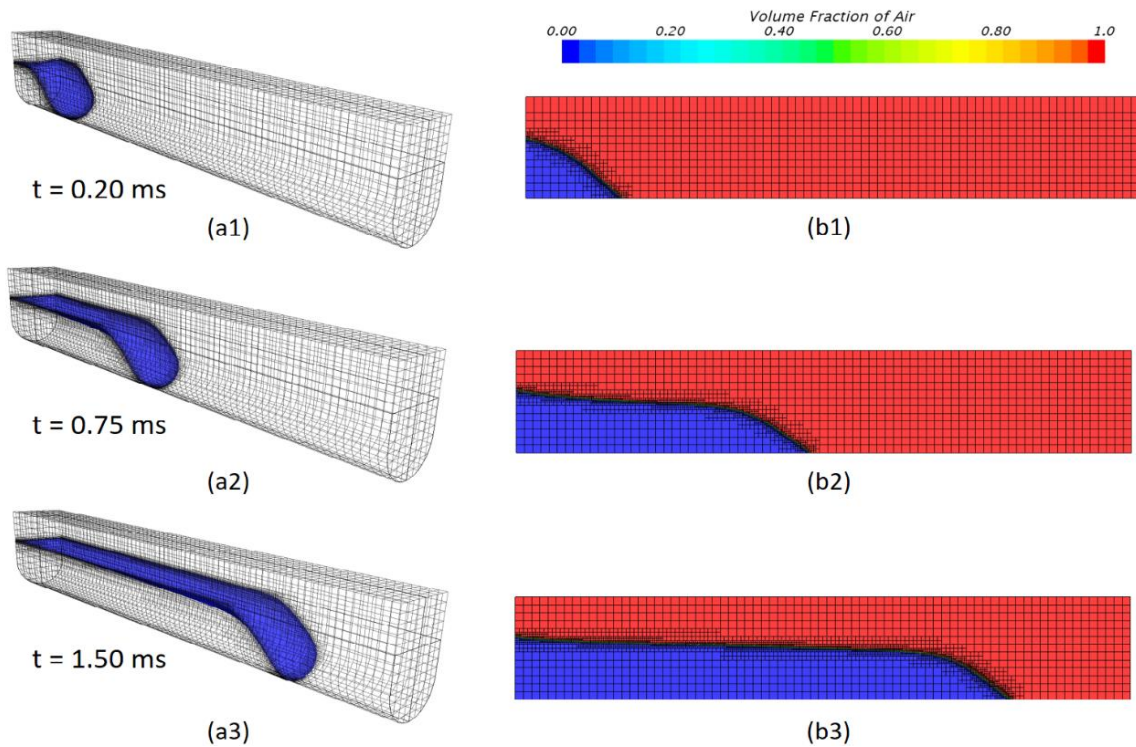
Figure 3. Mesh adaption in a U-shaped channel for three time values of 0.2, 0.75 and 1.5 ms. (a): 3D view representation of the water-air interface (b) volume fraction of air profile at the channel center.

This approach helped reducing the computational effort and the simulation run-time drastically and the computational grid was refined by 50 times at the gas-liquid interface, providing results with higher quality.

2.3   MODEL VALIDATION

An analytical model was derived by Yang et al.[21] for tracking the location of the

meniscus in open rectangular channels using the similar force balance that was employed

in the derivation of the Lucas-Washburn equation[8][9]. They assumed that the channel is

completely filled from the entry up to the meniscus and the contact angle at the channel

walls and the shape of the advancing meniscus are constant. They showed that the squared

of the meniscus position changes linearly with time:

$$x^2 \approx k \times t \tag{23}$$

where x is the meniscus location, t is the time and k is a mobility parameter that only

depends on the channel cross-section, aspect ratio ($p = \frac{w}{d}$), the viscosity (μ) and surface

tension (γ) of the liquid.

$$k = \frac{2\gamma d}{\mu} \frac{[2\cos\theta - (1-\cos\theta)p]}{p^2} g(p) \tag{24}$$

Where d is the channel depth and

$$g(p) = \frac{128}{\pi^5} \sum_{n\geq 0,\, odd}^{\infty} \frac{1}{n^5} \left(\frac{n\pi}{4} p - \tanh\frac{n\pi}{4} p\right) \tag{25}$$

Equation 24 is valid when the full slip boundary condition holds at the gas-liquid interface.

Note that the full slip boundary at the interface is usually valid for clean systems [36],

nevertheless, the presence of a minor contamination or surfactants in the system can

immobilize this boundary[37][38]. Figure 4 provides a comparison between how the

analytical and the numerical model predict the meniscus location in an open rectangular

microchannel. The channel is 20 μm wide, 20 μm deep (p=1) and 500 μm long. Three

different levels of adaptive refinement were used ($\Delta x = 0.5$ μm, $\Delta x = 1$ μm and $\Delta x =$

1.5 μm) to determine how the model predictions depend on the grid. As is shown in Figure

4 the analytical solution over-predicts the meniscus location compared to our numerical results. Various microfluidic studies that have shown that the actual flowrate inside the channels is smaller than what is predicted theoretically[28][29] [39][40][41]. This deviation can be justified if we reconsider the assumptions made for deriving of the analytical model. First, it was assumed that the channel is completely filled with the liquid
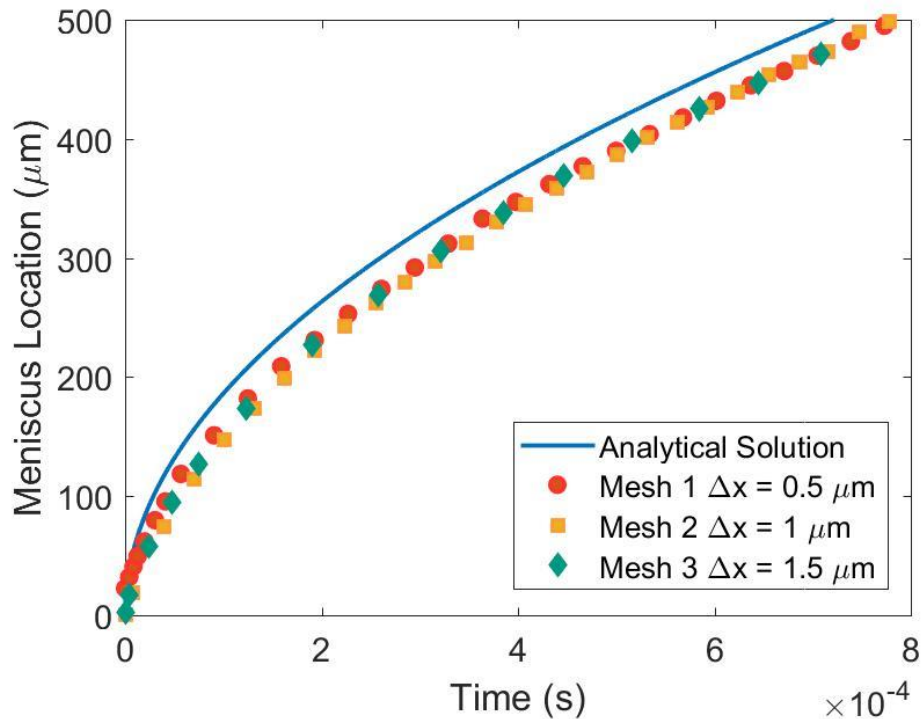
Figure 4. Model Validation based on the analytical solution[21] for three different levels of adaptive mesh refinement in a rectangular microchannel.

from the entry up to the meniscus. This assumption completely neglects the meniscus morphology and its concave profile. Thanks to the concave profile of the meniscus, only a partial portion of the channel is filled with the liquid, where the velocity gradient is much higher compared to the other portion of the channel where the channel is completely filled. As a result, the drag due to shear stress becomes significantly higher at the partially filled

portion of the channel, which reduces the flowrate compared to what the analytical model predicts. The model also fails to consider the dynamics of the contact angle and assumes a constant value for the contact angle. However, this assumption does not seem to have a significant effect on the capillary flow and the meniscus location as proposed by Mitra and Saha[15]. Minor discretization errors can also be a reason for this deviation. However, based on the mesh sensitivity analysis provided in Figure 4, we can conclude that our model predicts the meniscus location independent of the mesh element size.

3.   RESULTS AND DISCUSSION

3.1   SCF CRITERIA

The condition for Spontaneous Capillary-driven Flow was derived for different microchannel geometry in Table 1. In this section, the criteria for Spontaneous Capillary-driven flow is analyzed numerically for rectangular, circular, U-shaped and V-shaped channels. A user-defined field function (UDF) was employed to initialize all the cases so that the channels are initially filled by liquid water, only 2 μm away from the inlet with the initial velocity of zero. The contact angle was initially set to a high value for each case and was decreased until spontaneous flow was observed. Figure 5 shows the analytical and the numerical critical contact angle below which the liquid will spontaneously flow inside the channel for different geometries. The red line predicts the critical contact angle based on the analytical derivation presented in Table 1. The spontaneous flow occurs in the area colored by yellow and for all the cases above the red line, there will be no flow due to capillary action. The dashed blue line represents the predicted critical contact angle based on the numerical simulation.
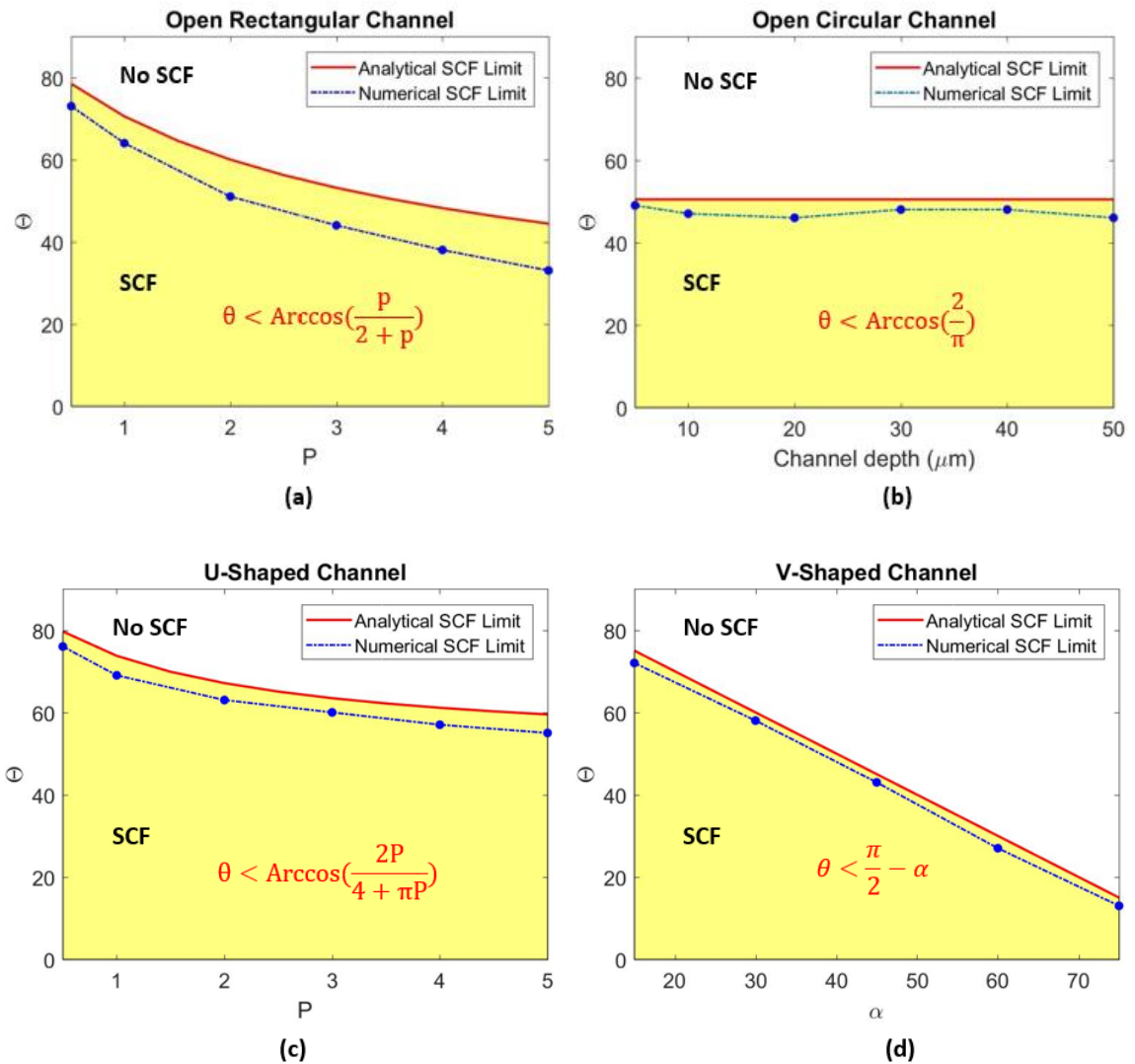
Figure 5. Comparison between the numerical and analytical SCF limit in different channels. (a) Open rectangular channel (b) Open circular channel (c) U-shaped channel (d) V-shaped channel.

There is a good agreement between the analytical and numerical results. Nevertheless, in all the cases studied the numerical SCF limit is somewhat smaller than what is predicted analytically. This can be justified considering that in the derivation of the analytical SCF condition, it was readily assumed that the channel is completely filled

with the liquid and the morphology of the meniscus was ignored. Let us reconsider the

SCF condition $\frac{dA_{LG}}{dA_{SL}} < \cos(\theta)$: Due to the morphology of the meniscus and its concave

profile, dA_{LG} increases as the gas-liquid interface curvature increases over the time.

Nevertheless, the increase in dA_{SL} is minor compared to the increase of dA_{LG} and as a

result, the left side term in the CSF criteria increases which causes the critical contact angle

to decrease. The two corners inside an open rectangular channel result a higher curvature

for the gas-liquid interface and a more deviation from the assumption of a completely filled

channel and as it is shown in Figure 5a, the numerical results predict a smaller contact

angle below which the spontaneous flow occurs. In an open rectangular channel and a U-

shaped channel, the SCF limit mainly depends on the aspect ratio (p) of the channel, where

as in an open circular channel, the critical contact angle is almost constant and independent

of the channel depth (width). In a V-shaped channel, the critical contact angle is only a

function of the bottom dihedral angle (α) and decreases linearly with the increase of α. Note

that for cases with very small side walls in a U-shaped channel, P becomes sufficiently

large and the term $Arccos(\frac{2p}{4+\pi p})$ becomes equal to $Arccos\left(\frac{2}{\pi}\right)$, which is the exact SCF

condition for an open circular channel.

3.2 MOBILITY PARAMETER

In this section, the effect of geometry on the spontaneous flow has been analyzed

and the developed numerical model is used to predict the advancing meniscus in an open

rectangular, circular, U-shaped and a V-shaped channel. The open channel's depth vary

from 10 to 80 μm and in all the cases, they are 1.5 mm long. The contact angle is considered

to be constant and equal to 20°. An iso-surface was defined at the channel center line to

track the front meniscus with time. The minimum level of grid refinement was altered based on the channel dimensions to avoid an excess number of computational cells. The change of the advancing meniscus location with time are presented in Tables 1-16 in Appendix.

Figure 6 represents the profile of the volume fraction of air at the center of an open rectangular, open circular, V-shaped and U-shaped channel with a depth of 80 μm and a length of 1.5 mm at different time values. It is visually observed in Figure 6 that the channel filling rate is the lowest and highest in a V-shaped and a U-shaped channel, respectively.
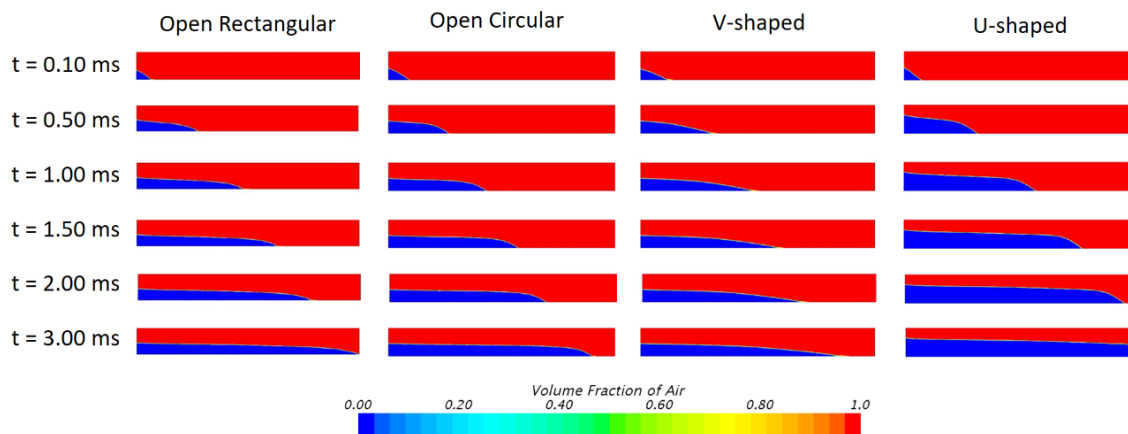
Figure 6. Transient profile of the volume fraction of air at the center of different microchannels with a depth of 80 μm and a length of 1.5 mm.

The advancing meniscus location has been plotted in Figure 7 for different channels. The slope on these curves represent the filling velocity in the microchannel and it can be observed that there is an increase in the filling velocity with the increase of the channel depth. This increase seems to be a lot more significant in a U-shaped channel. Figure 8 shows how the squared location of the advancing meniscus change with time for

different channels with different depths. As it was demonstrated in the previous chapter,

the squared of the meniscus location is expected to increase linearly with time and satisfy
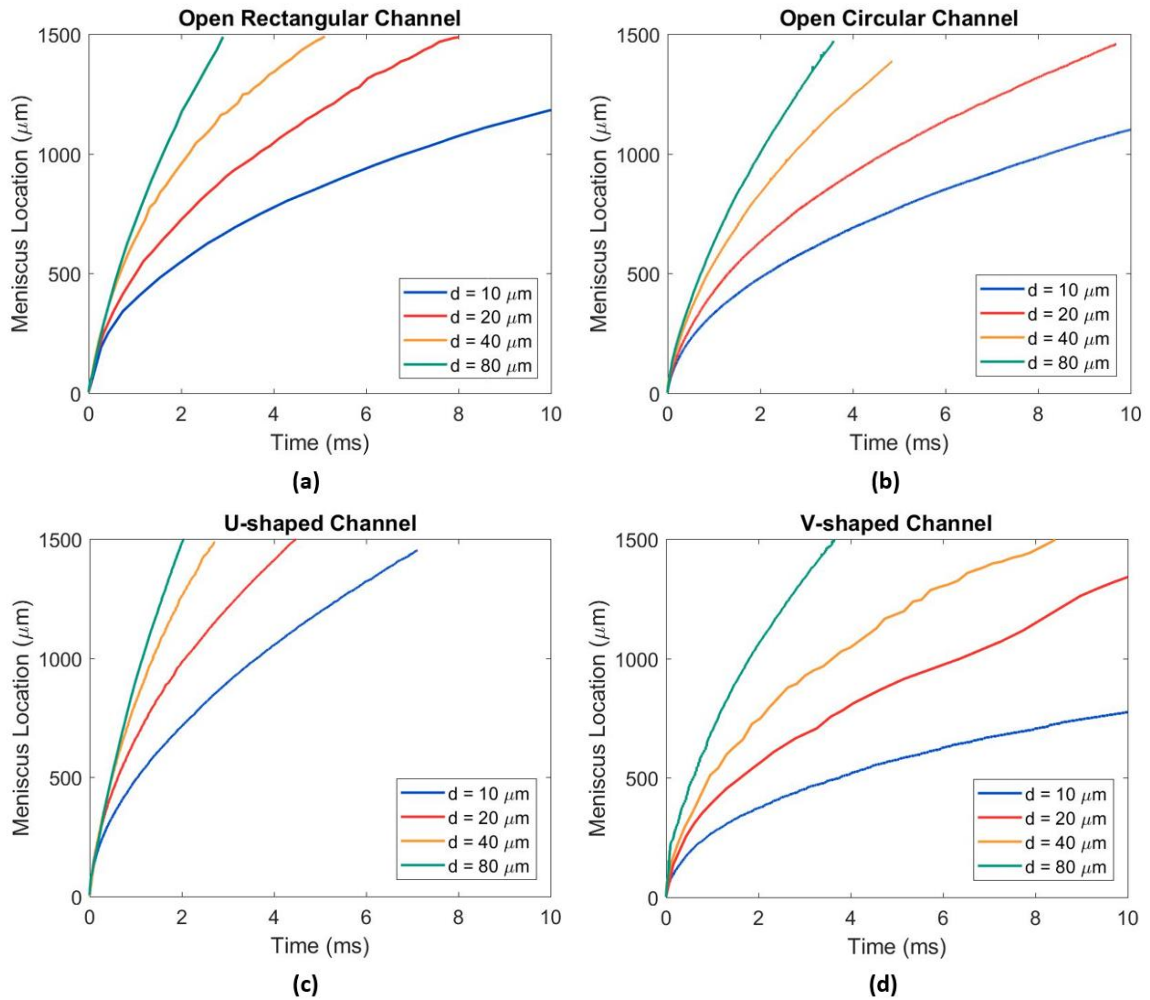
Figure 7. Advancing meniscus location in open microchannels of different geometry for different channel depths. (a) Open Rectangular Channel, (b) Open Circular Channel, (c) U-shaped Channel, (d) V-shaped Channel ($\alpha = 45°$).

the Lucas-Washburn behavior. We refer to the slope of this linear behavior as the "Mobility

parameter" k. The effect of the microchannel geometry on the mobility parameter is

important for determining how fast the meniscus location changes with time. It is observed

in Figure 8 that this linear behavior starts after a short interval of t_0. The precise value of t_0 is hard to determine in experiments and in most cases where the overall time t is much larger than t_0, this value is neglected. t_0 can be determined by finding the intercept of the time axis, based on a linear regression:

$$x^2 = k \times (t - t_0) \tag{26}$$

The value of t_0 is in the order of 0.1 to 0.3 milliseconds and increases with the increase of channel depth, regardless of the geometry of the microchannel. As it is shown in Figure 8 the linear fit agrees well with what our computational model predicts and the coefficient of determination (R^2) is higher than 0.9867 for all the cases studied. R^2 is equal to 1 for small channel depths and as the depth increase, there is a minor decrease in the value of R^2. This is due the fact that the channel depth has been increased, yet the channel length was kept constant, therefore, the length of the channels is not long enough for the flow to become fully developed and for the surface tension force and the viscous resistance force to balance each other. As a result, it is recommended to keep the channel length to depth ratio constant in the future case studies. The mobility parameter for all of the case studies have been compared in Figure 9. In all the geometries studied, with the increase of the channel depth, the mobility parameter increases and therefore, the advancing meniscus location increases faster. This results agree well with the laminar Poiseuille flow behavior and the observations of Kuo et al. [17] in their experiments. To justify this behavior, let us consider the flow behavior in a simple cylindrical channel where according to Poiseuille's law the flow velocity can be determined as:

$$u(r) = \frac{\Delta P}{4 \mu L} \times R^2 (1 - \left(\frac{r}{R}\right)^2) \tag{27}$$
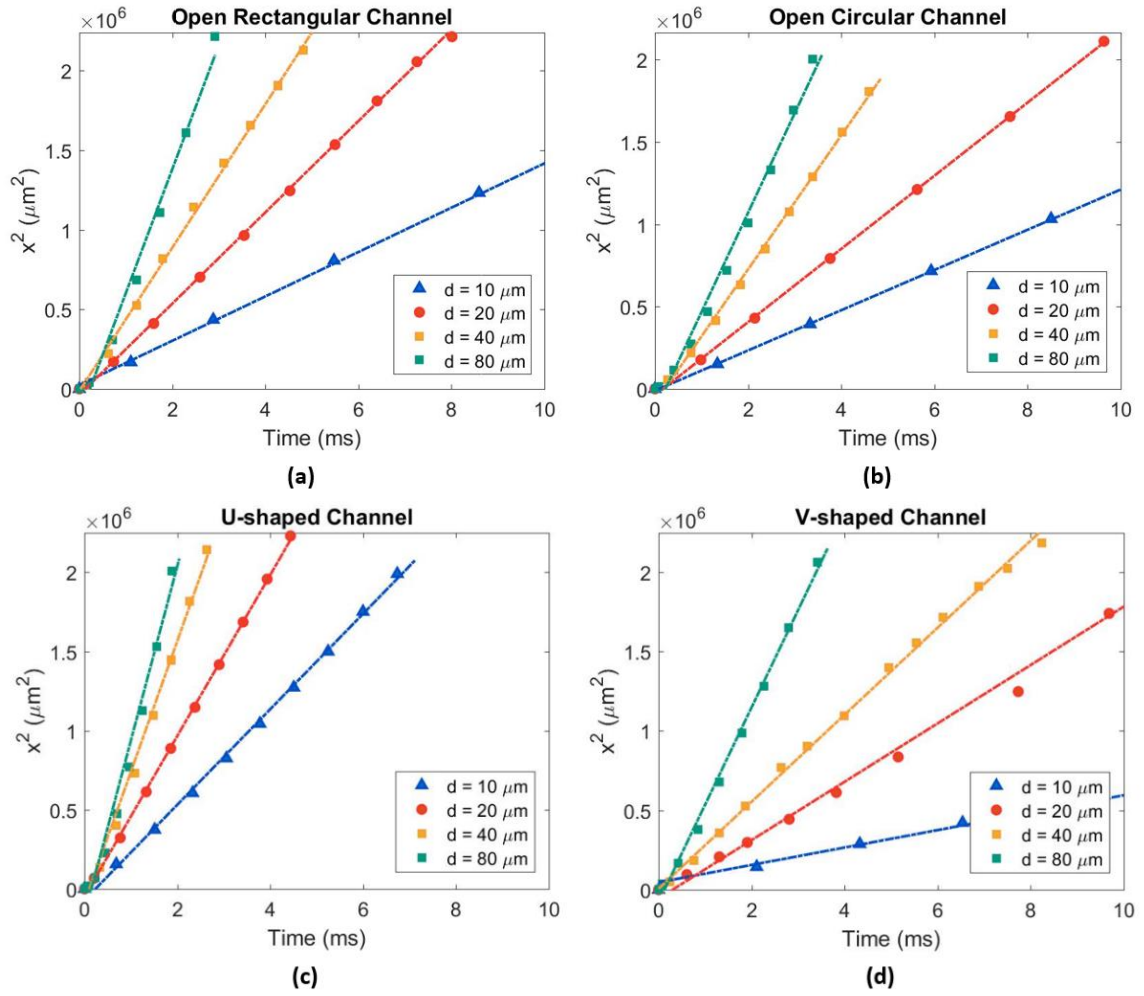
Figure 8. The squared of the advancing meniscus location in open microchannels of different geometry for different channel depths. (a) Open Rectangular Channel, (b) Open Circular Channel, (c) U-shaped Channel, (d) V-shaped Channel ($\alpha = 45°$).

where $u(r)$ is the fluid velocity in the axial direction at the radius r, ΔP is the liquid pressure drop, L is the channel length, R is the full channel radius and μ is the dynamic viscosity of the liquid. Thus we can find:

$$u(r) \sim \Delta P \times R^2 \tag{28}$$

On the other hand, the pressure difference can be determined using Laplace Equation:

$$\Delta P = \frac{2\gamma \cos(\theta)}{R} \tag{29}$$

where R is the channel radius, γ is the surface tension, θ is the contact angle and R is the channel radius. If we consider Equation 29, there is an increase in the pressure difference with the decrease of the channel radius (depth). Nevertheless, $u(r)$ is proportional to the squared of channel depth and the channel depth decrease overcompensates the increase of the pressure difference and therefore, the velocity decreases.
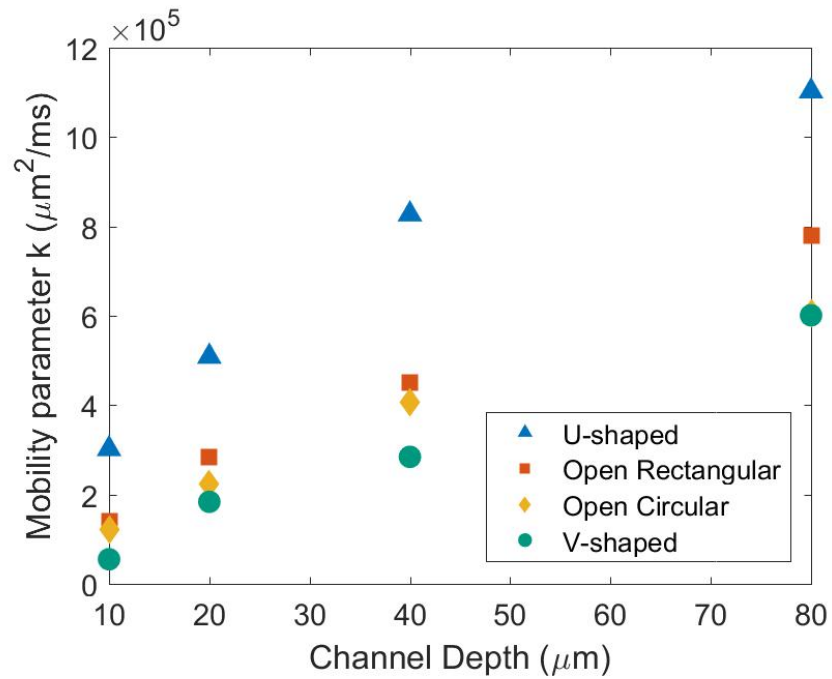
Figure 9. Mobility parameter comparison for different channels of different depths.

It is also observed in Figure 9 that the meniscus moves much faster in a U-shaped channel compared to other channel geometries. Given that the channel cross-sectional area in a U-shaped channel is higher compared to a rectangular, circular and V-shaped channel of the same depth size, the mass flow rate in a U-shaped channel will be significantly higher than other geometries (see Figure 10). Figure 11 represents the H2Ri Geotextile that

contains thousands of hydrophilic open microchannels that allow capillary flow to drain

and transport water out of the soil.
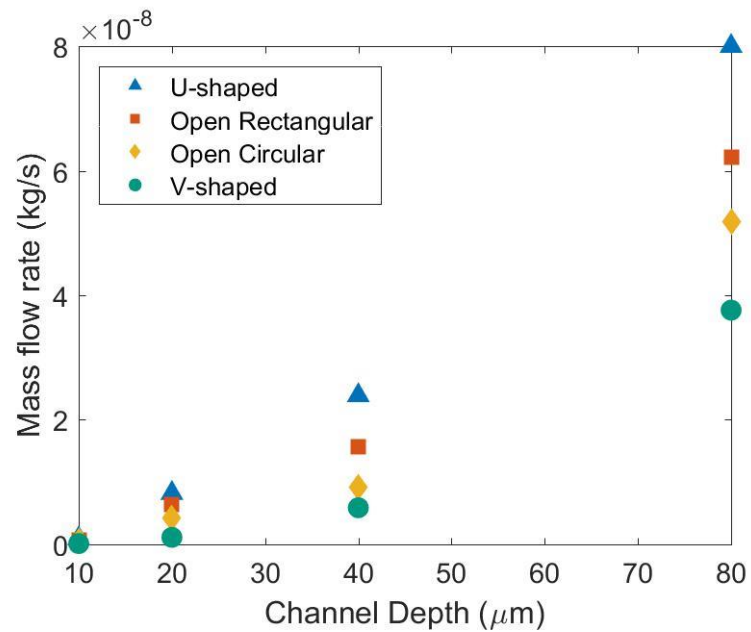
Figure 10. Comparison of the liquid mass flow rates based on the microchannel depth and type.
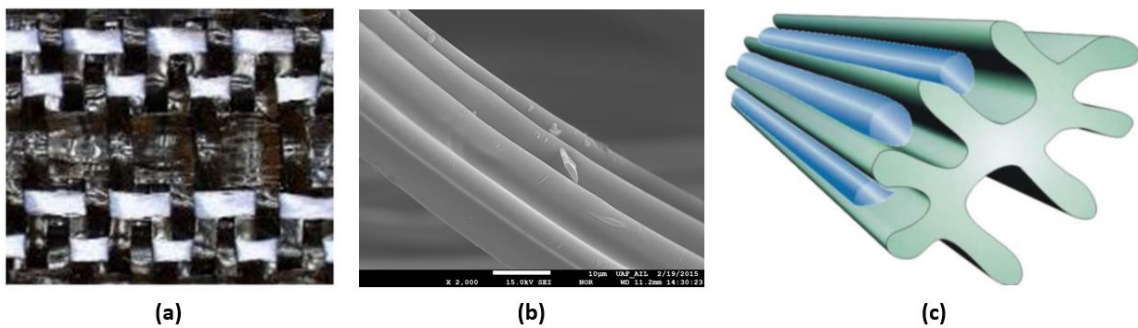
Figure 11. H2Ri Geotextile. (a) Image of four adjacent threads in a Geotextile (b) SEM image of a single H2Ri fiber containing eight open microchannels (c) Schematic representation of the capillary-driven flow in a single wicking fiber[42].

If we consider the H2Ri Geotextile, the 17 cm wide fiber consists of 64 threads and each thread is estimated to contain 200 hydrophilic fibers. Considering that each individual fiber is made out of about eight open microchannels, given the water mass flow rate of 4.5×10^{-9} kg/s for an 15 μm U-shaped channel, on a daily basis, the wicking fabric is capable of transporting about 234 kg of water per day. However, the water mass flowrate in the wicking fabric that was measured experimentally for saturated soils was found to be relatively higher, but in the same order of magnitude and about 879 kg of water per day. This reasonable deviation can be justified considering the interactions between the hydrophilic fibers when they are compressed all together in the manufacturing process of the geotextile, also known as the grouping effect. This would result in channels with irregular cross-sections and more number of open microchannels per one individual fiber, as well. The experimental results highly depend on temperature variations and the relative humidity of air, whereas the computational model neglects the evaporation of the water inside the open microchannels. Due to the small time scale, a quasi-steady state is assumed for the energy inside the control volume and the temperature variations of the fluid has been neglected.

3.3   NEGATIVE INLET PRESSURE

According to the second law of thermodynamics, if a process generates Entropy, the less energy will be available to do useful work and if a process generates Entropy or in other words, occurs spontaneously, it will be irreversible as long as you input more energy to the system. As demonstrated in the previous section, the liquid flows inside the microchannels when the inlet pressure is higher than the menisci pressure. The theoretical

concept of soil suction was developed in the early 1900's [42]. Historically, soil mechanics theory has been more concerned with saturated soils where the pores between soil particles are temporarily or permanently filled with water. The pore water pressure in saturated soils generally positive and it is a function of the depth, the specific weight of water and the drainage conditions. However, in unsaturated soils where the pores and filled with air as well as water, above the water table, the capillary force between the soil particles draw the water upwards. These molecular, physical-chemical forces acting at the water-soil particles boundary gives the soil above the water table an attraction for water which is known as soil suction and is represented as negative pore water pressure [43]. As represented in Figure 12, when the surface of the soil is air dried, the water transport to outside of the soil is blocked just as if an impermeable membrane exists on the surface. The precipitation and the capillary rise of water above the water table results an accumulation of water and increase in the soil water content and reduces the its strength. In this section, the effect of the negative pore water pressure as the input work to make the spontaneous process reversible is studied by setting a negative pressure boundary at the microchannel inlet in a U-shaped, V-shaped, open rectangular and open circular microchannels (Figure 13).
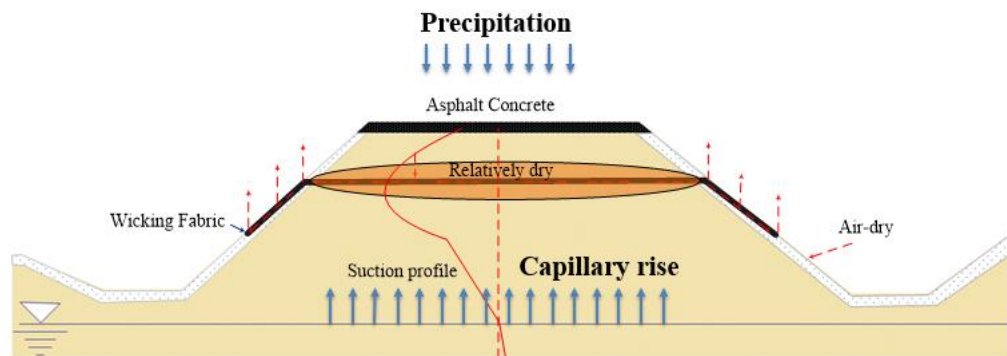
Figure 12. Mechanism of water drainage from unsaturated soils using the wicking fabric.

In all case studies, the microchannels are only partially filled with the liquid water as an initial condition. The inlet pressure was decreased sequentially to find the minimum negative inlet pressure at which spontaneous flow occurs. To increase the numerical stability of the solver and given the interest in the liquid flow behavior, the density of the gas phase (air) was set to $100 \frac{kg}{m^3}$.
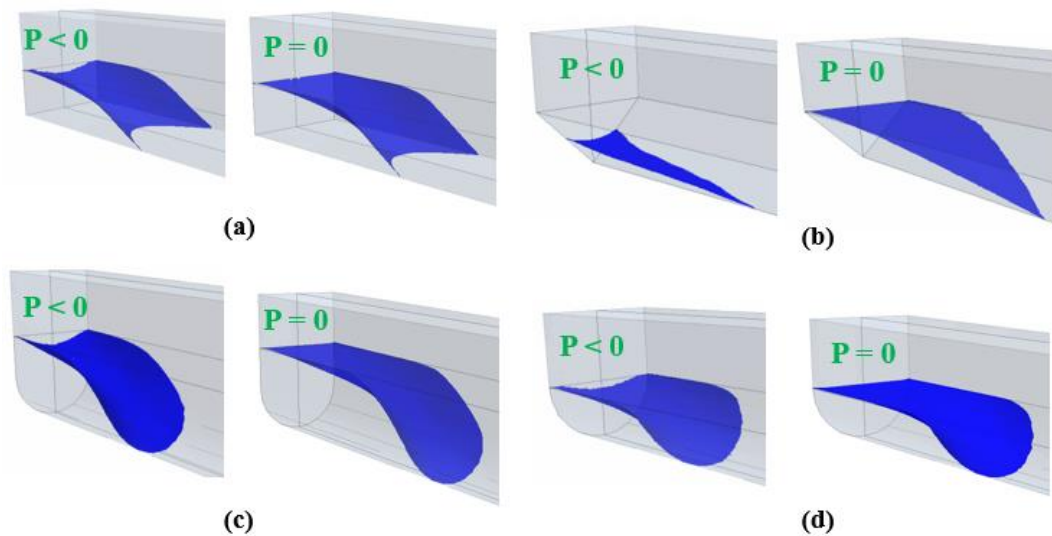
Figure 13. The effect of negative inlet boundary pressure on the advancing mensicus in different channel geometries: (a) Open rectangular microchannel, (b) V-shaped microchannel, (c) U-shaped channel, (d) Open Circualr micochannel.

This approach helped a lot with reducing the very high backflow of air into the negative pressure boundary which caused divergence of the solver or reduced the time step size by two orders of magnitude. A sensitivity analysis was conducted to determine this assumption affected the numerical results and the critical negative inlet pressure (see Figure 14). First, the density of the gas phase was set to $1.184 \frac{kg}{m^3}$ (Figure 14a), which is the actual density of air. The low density of the gas combined with relatively high negative

inlet pressure caused the model to predict unphysical high velocities inside the microchannel. This adversely reduced the adaptive time step to 4×10^{-9}s.
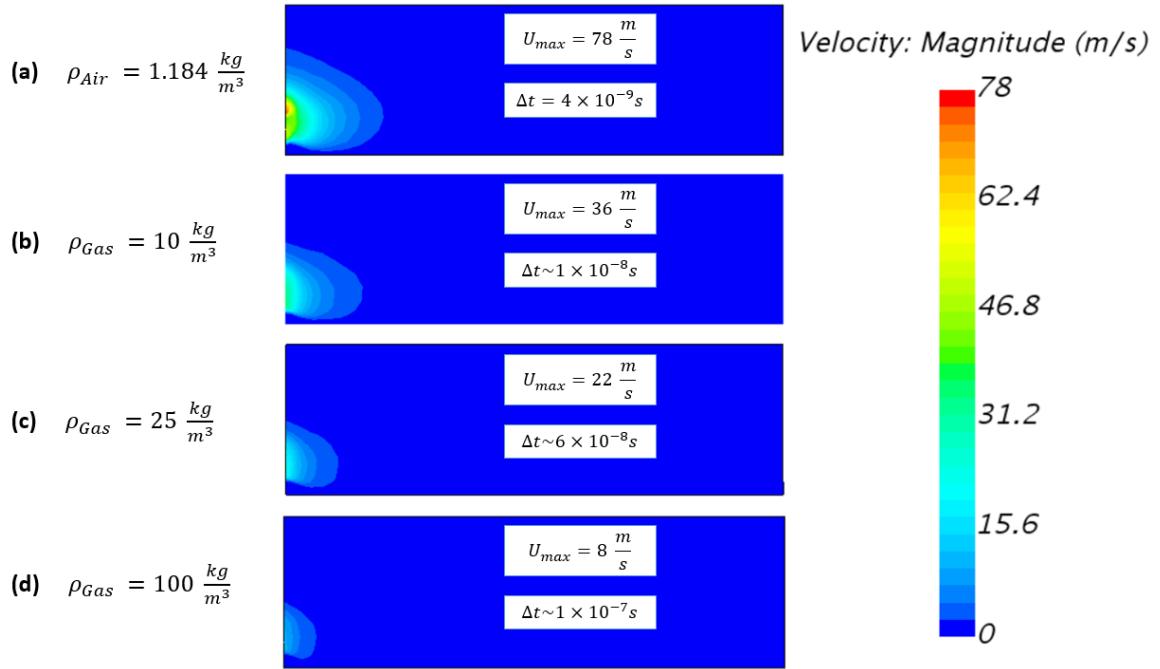
Figure 14. Velocity magnitude profiles at the central cross-section of a 10 μm U-shaped microchannel . Air density is set to (a) 1.184 $\frac{kg}{m^3}$, (b) 10 $\frac{kg}{m^3}$, (c) 25 $\frac{kg}{m^3}$ and (d) 100 $\frac{kg}{m^3}$.

The density of the gas phase was sequentially increased and the corresponding maximum velocities, time step and the critical negative pressures were compared. It was found that the gas density of 100 $\frac{\text{kg}}{\text{m}^3}$ resulted a reasonable time step values and predictions for the back flow velocity. The critical negative inlet pressure for all the cases studied was found to be almost constant and independent of the gas phase density.

The change in the minimum inlet pressure with the channel depth for different microchannel geometries is represented in Figure 15. The minimum pressure at which there

is stop in the liquid flow are represented as points and at any higher inlet pressure, the liquid water spontaneously flows inside the microchannel. It is observed that a V-shaped channel can provide spontaneous flow at relatively lower minimum inlet pressure compared to the other geometries.
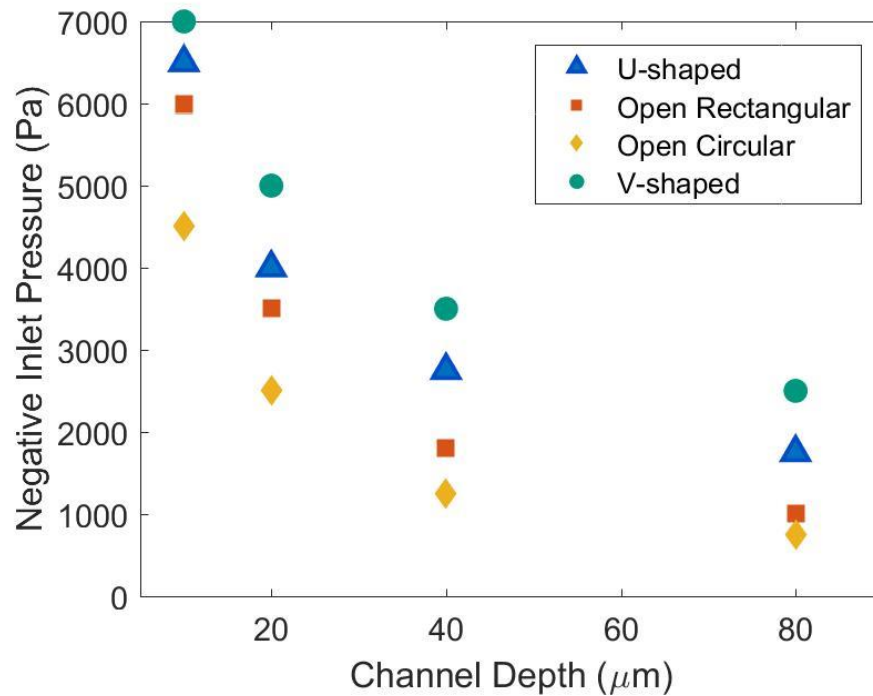
Figure 15. Change of the minimum negative inlet pressure with the channel depth for spontaneous flow in different microchannel geometries.

As observed in Figure 15, in all the cases studied, the absolute minimum inlet pressure for the spontaneous flow decreases with the increase of the channel depth, regardless of the geometry type. This behavior can be justified considering the Laplace equation (Equation 29) where the pressure difference is proportional to the reversed of the channel radius (depth), resulting a higher pressure difference for smaller microchannels.

4. CONCLUSIONS

In this study, the behavior of spontaneous capillary-driven flow has been investigated numerically using the Volume-of-Fluid (VOF) method. While a sharp gas-liquid interface was not captured in the former numerical microfluidic studies due to employment of an overall coarse grid to reduce the computational effort, a grid adaption algorithm was developed in this work to refine the mesh at the gas-liquid interface only and minimize the computational time. The algorithm developed allows using an overall coarse grid but refines the mesh at the moving interface, which is very promising for channels of high length to depth ratio. Analytical conditions were derived and compared with the numerical criteria for determining the maximum contact angle for the spontaneous flow for different channel geometries based on channel properties. Considering the critical contact angle, it was found that U-shaped channels provide a much wider choice of material to ensure spontaneous flow compared to the other microchannel geometries. The advancing meniscus location was reported with time and the filling velocities of the wetting fluid was found to increase with the channel's depth regardless of the microchannel geometry. Among the studied geometries, U-shaped channels were found to have significant higher filling velocity and mass flow rate. The minimum inlet pressure which the liquid water spontaneously flows inside the channel was determined numerically. Amongst the geometries studied, it was observed that a V-shaped channel provides the spontaneous flow at a lower minimum pressure and is more applicable to higher soil suctions at the expense of having the lowest water mass flow rate. The numerical model developed is valid and applicable for a wide range of geometric configurations and boundary conditions. The

results of this study can be applied to the microfluidics system design in different fields of

science and engineering.

REFERENCES

[1]   Y.-F. Tsai, C.-J. Shieh, and H. Yang, "Capillary force pumping fluid for glucose oxidase enzymatic fuel cells," Microsyst. Technol., vol. 23, no. 9, pp. 3927–3935, 2017.

[2]   J. P. McHale and S. V Garimella, "Heat transfer in trapezoidal microchannels of various aspect ratios," Int. J. Heat Mass Transf., vol. 53, no. 1–3, pp. 365–375, 2010.

[3]   K.-Y. Weng, N.-J. Chou, and J.-W. Cheng, "Triggering vacuum capillaries for pneumatic pumping and metering liquids in point-of-care immunoassays," Lab Chip, vol. 8, no. 7, pp. 1216–1219, 2008.

[4]   C. D. Chin, S. Y. Chin, T. Laksanasopin, and S. K. Sia, "Low-cost microdevices for point-of-care testing," in Point-of-care Diagnostics on a chip, Springer, 2013, pp. 3–21.

[5]   D. G. Gilmore and M. Bello, Satellite thermal control handbook, vol. 1. Aerospace Corporation Press EI Segundo, CA, 1994.

[6]   Y. Tang, X. Chen, and Y. Huang, "Capillary flow rate limitation in asymmetry open channel," Chinese J. Aeronaut., vol. 28, no. 3, pp. 720–728, 2015.

[7]   C. Lin and X. Zhang, "A Bio-Wicking System to Mitigate Capillary Water in Base Course," 2016.

[8]   R. Lucas, "Ueber das Zeitgesetz des kapillaren Aufstiegs von Flüssigkeiten," Kolloid-Zeitschrift, vol. 23, no. 1, pp. 15–22, 1918.

[9]   E. W. Washburn, "The dynamics of capillary flow," Phys. Rev., vol. 17, no. 3, p. 273, 1921.

[10]   C. H. Bosanquet, "LV. On the flow of liquids into capillary tubes," London, Edinburgh, Dublin Philos. Mag. J. Sci., vol. 45, no. 267, pp. 525–531, 1923.

[11]   S. W. Tchikanda, R. H. Nilson, and S. K. Griffiths, "Modeling of pressure and shear-driven flows in open rectangular microchannels," Int. J. Heat Mass Transf., vol. 47, no. 3, pp. 527–538, 2004.

[12] N. Ichikawa, K. Hosokawa, and R. Maeda, "Interface motion of capillary-driven flow in rectangular microchannel," J. Colloid Interface Sci., vol. 280, no. 1, pp. 155–164, 2004.

[13] L. J. Yang, T. J. Yao, and Y. C. Tai, "The marching velocity of the capillary meniscus in a microchannel," J. Micromechanics Microengineering, vol. 14, no. 2, pp. 220–225, 2004.

[14] Y. Chen, L. S. Melvin, S. Rodriguez, D. Bell, and M. M. Weislogel, "Capillary driven flow in micro scale surface structures," Microelectron. Eng., vol. 86, no. 4–6, pp. 1317–1320, 2009.

[15] A. Ashish Saha and S. K. Mitra, "Effect of dynamic contact angle in a volume of fluid (VOF) model for a microfluidic capillary flow," J. Colloid Interface Sci., vol. 339, no. 2, pp. 461–480, 2009.

[16] Y. Zhu and K. Petkovic-Duran, "Capillary flow in microchannels," Microfluid. Nanofluidics, vol. 8, no. 2, pp. 275–282, 2010.

[17] M. Chip, J. Kuo, W. Lee, J. Chen, J. K. Ã, and Y. Lin, "Capillary-Driven Dynamics of Water in Hydrophilic Microscope Coverslip Nanochannels Capillary-Driven Dynamics of Water in Hydrophilic Microscope Coverslip Nanochannels," 2012.

[18] S. Cito, J. Pallares, A. Fabregat, and I. Katakis, "Numerical simulation of wall mass transfer rates in capillary-driven flow in microchannels," Int. Commun. Heat Mass Transf., vol. 39, no. 8, pp. 1066–1072, 2012.

[19] F. F. Ouali, G. McHale, H. Javed, C. Trabi, N. J. Shirtcliffe, and M. I. Newton, "Wetting considerations in capillary rise and imbibition in closed square tubes and open rectangular cross-section channels," Microfluid. Nanofluidics, vol. 15, no. 3, pp. 309–326, 2013.

[20] M. Furrer, L. Saraceno, A. Mariani, and G. P. Celata, "Capillary pressure influence on open channels pressure drop," Int. J. Therm. Sci., vol. 70, pp. 102–113, 2013.

[21] D. Yang, M. Krasowska, C. Priest, and J. Ralston, "Dynamics of capillary-driven liquid–liquid displacement in open microchannels," Phys. Chem. Chem. Phys., vol. 16, no. 44, pp. 24473–24478, 2014.

[22] J. Berthier, K. A. Brakke, and E. Berthier, "A general condition for spontaneous capillary flow in uniform cross-section microchannels," Microfluid. Nanofluidics, vol. 16, no. 4, pp. 779–785, 2014.

[23] J. Berthier, D. Gosselin, and E. Berthier, "A generalization of the Lucas–Washburn–Rideal law to composite microchannels of arbitrary cross section," Microfluid. Nanofluidics, vol. 19, no. 3, pp. 497–507, 2015.

[24] I. Publishing et al., "S e n s o r s & T r a n s d u c e r s The Dynamics of Spontaneous Capillary Flow in Confined and Open Microchannels," vol. 183, no. 12, pp. 123–128, 2014.

[25] J. Berthier, K. A. Brakke, D. Gosselin, F. Navarro, N. Belgacem, and D. Chaussy, "Spontaneous capillary flow in curved, open microchannels," Microfluid. Nanofluidics, vol. 20, no. 7, pp. 1–9, 2016.

[26] J. Berthier et al., "On the halt of spontaneous capillary flows in diverging open channels," Med. Eng. Phys., vol. 48, pp. 75–80, 2017.

[27] P. J. Ponce De Leon and L. F. Velásquez-Garcia, "Optimization of capillary flow through open-microchannel and open-micropillar arrays," J. Phys. D. Appl. Phys., vol. 49, no. 5, 2016.

[28] T. W. Sowers, R. Sarkar, S. Eswarappa Prameela, E. Izadi, and J. Rajagopalan, "Capillary driven flow of polydimethylsiloxane in open rectangular microchannels," Soft Matter, vol. 12, no. 26, pp. 5818–5823, 2016.

[29] R. K. Lade, E. J. Hippchen, C. W. Macosko, and L. F. Francis, "Dynamics of Capillary-Driven Flow in 3D Printed Open Microchannels," Langmuir, vol. 33, no. 12, pp. 2949–2964, 2017.

[30] J. W. Gibbs, "A Method of Geometrical Representation of the Thermodynamic Properties by Means of Surfaces," Trans. Connect. Acad. Arts Sci., pp. 382–404, 1873.

[31] S. Middleman, An introduction to mass and heat transfer: principles of analysis and design. Wiley Online Library, 1997.

[32] C. W. Hirt and B. D. Nichols, "Volume of fluid (VOF) method for the dynamics of free boundaries," J. Comput. Phys., vol. 39, no. 1, pp. 201–225, 1981.

[33] J. U. Brackbill, D. B. Kothe, and C. Zemach, "A continuum method for modeling surface tension," J. Comput. Phys., vol. 100, no. 2, pp. 335–354, 1992.

[34] S. Patankar, Numerical heat transfer and fluid flow. CRC press, 1980.

[35] S. Muzaferija, "A two fluid Navier-Stokes solver to simulate water entry," in 21st Symposium on Naval Hydrodynamics, Berkeley, 1988, 1988.

[36] L. Parkinson, R. Sedev, D. Fornasiero, and J. Ralston, "The terminal rise velocity of 10–100 μm diameter bubbles in water," J. Colloid Interface Sci., vol. 322, no. 1, pp. 168–172, 2008.

[37] O. Manor, I. U. Vakarelski, G. W. Stevens, F. Grieser, R. R. Dagastine, and D. Y. C. Chan, "Dynamic forces between bubbles and surfaces and hydrodynamic boundary conditions," Langmuir, vol. 24, no. 20, pp. 11533–11543, 2008.

[38] O. Manor et al., "Hydrodynamic boundary conditions and dynamic forces between bubbles and surfaces," Phys. Rev. Lett., vol. 101, no. 2, p. 24501, 2008.

[39] J. M. Oh, T. Faez, S. de Beer, and F. Mugele, "Capillarity-driven dynamics of water–alcohol mixtures in nanofluidic channels," Microfluid. Nanofluidics, vol. 9, no. 1, pp. 123–129, 2010.

[40] J. Haneveld, N. R. Tas, N. Brunets, H. V Jansen, and M. Elwenspoek, "Capillary filling of sub-10 nm nanochannels," J. Appl. Phys., vol. 104, no. 1, p. 14309, 2008.

[41] M. N. Hamblin et al., "Capillary flow in sacrificially etched nanochannels," Biomicrofluidics, vol. 5, no. 2, p. 21103, 2011.

[42] L. Richards, "Physical Condition of Water in Soil 1," Methods Soil Anal. Part 1. Phys. Mineral. Prop. Incl. Stat. Meas. Sampl., no. methodsofsoilana, pp. 128–152, 1965.

[43] A. M. Ridley, "Soil suction—what it is and how to successfully measure it," 2015.

SECTION

5.   CONCLUSIONS

In this work, the capability of the wicking fabric for draining water from soil was analyzed numerically by modeling and predicting the fluid flow behavior inside the wicking fibers as open microchannels using the finite volume analysis and computational fluid dynamics (CFD).   Two algorithms were developed to adapt the grid and the time step that increased the numerical stability of the solver and reduced the computational cost, as well. The model was verified based on an analytical solution found in the literature and is valid for other future case studies with different geometries or boundary conditions. Four different geometries were considered for the open microchannel: Rectangular, Circular, U-shaped and V-shaped. The analytical and numerical criteria for the spontaneous flow were determined based on the channel type and aspect ratio. The meniscus location and the filling velocities of the microchannels were determined and compared numerically in term of the mobility parameter. U-shaped channels were found to have the highest filling velocity and also provide a wider choice of material for design in terms of the critical contact angle for spontaneous flow. The effect of the negative inlet pressure on the spontaneous flow was also analyzed by considering a negative pressure boundary at the microchannel inlet and the maximum negative pressure that allows the spontaneous flow was determined numerically for different channel geometries. In another approach, the density of the gas phase was increased which reduced the back flow and increased the numerical stability of the solver. The results and findings in this work can provide comprehensive information on the design considerations of microfluidic devices.

6.   FUTURE WORK

The developed numerical model can be applied to any further study in the future with different geometry, boundary and initial condition. The deployment of adaptive mesh refinement and the adaptive time step algorithm makes this numerical model very promising for case studies with high channel length to depth ratio in terms of simulation run-time. In this work, the temperature variations and the effect of evaporation on the spontaneous flow has been neglected and the energy was assumed to follow a quasi-steady state behavior inside the control volume due the very small time scale of the analysis. The model verification was based on an assumption of isothermal flow, thus, further validations may be required in case of modeling evaporation inside the channels with the assumption of ideal gas law for the gas phase. In this work, the length of the microchannels were set to 1.5 mm for consistency. In the future studies, however, it is recommended to keep the channel length to depth ratio constant so that the flow is fully developed within the corresponding channel length. To avoid divergence and reduce the back flow at the inlet due to the negative pressure, a user-defined conditional boundary condition was defined at the inlet to set the pressure negative where liquid volume fraction was less than 0.5. However, this approach resulted unphysical behavior predictions of the flow. Since the main interest and focus of this study is in the liquid phase, in another approach the density of the gas phase was increased. This helped a lot with the stability of the numerical solver and was also found to have minor effects on the results of the analysis. However, in the future studies, it is highly recommended to extend the channel's inlet by a very small value and assign a confined wall boundary condition there.

APPENDIX

The change of the advancing meniscus location with time are presented in Tables 1-16.

Table 1. Meniscus location at different time values in an open rectangular channel (d=10 μm).

Time (ms)	Meniscus Location (μm)	Time (ms)	Meniscus Location (μm)
0.060811	76.5625	2.723059	641.5625
0.242836	180.3125	2.845192	656.5625
0.300967	209.6875	2.97267	669.6875
0.364538	235.3125	3.096588	683.4375
0.427838	252.8125	3.220585	698.4375
0.49332	275.3125	3.428685	721.5625
0.556437	285.9375	3.668719	745.9375
0.623344	314.0625	3.913107	767.1875
0.68995	327.1875	4.162802	791.5625
0.758822	341.5625	4.404634	814.0625
0.926383	375.3125	4.645862	834.6875
1.092343	406.5625	4.882914	849.6875
1.235997	432.1875	5.127923	867.8125
1.423823	470.9375	5.361768	890.9375
1.601755	492.1875	5.641419	912.1875
1.759717	515.3125	5.937073	935.3125
1.903239	534.6875	6.200627	952.8125
2.045753	555.3125	6.463518	972.1875
2.193715	575.3125	6.702652	989.6875
2.329838	591.5625	6.921747	1004.062
2.463775	610.9375	7.171703	1018.438

Table 2. Meniscus location at different time values in an open rectangular channel (d=20 μm).

Time (ms)	Meniscus Location (μm)	Time (ms)	Meniscus Location (μm)
0.004721	14.6875	2.546537	827.8125
0.027449	43.4375	2.664111	849.6875
0.127923	133.75	2.780142	868.4375
0.247457	210.9375	2.903266	893.4375
0.371881	271.5625	3.030436	909.0625
0.503689	328.4375	3.14248	931.5625
0.640214	381.25	3.268001	944.6875
0.757685	419.375	3.397982	966.5625
0.883456	456.875	3.523459	980.9375
0.982361	488.125	3.646627	999.0626
1.064431	513.4375	3.771508	1016.562
1.148397	539.6875	3.829793	1024.688
1.255641	565.9375	3.830584	1024.688
1.379951	591.5625	3.832417	1024.688
1.521714	618.4375	3.832289	1024.688
1.659084	649.6875	3.833116	1024.688
1.781528	681.5625	3.833807	1024.688
1.918194	710.9375	3.834428	1024.688
2.048588	733.4375	3.835139	1024.688
2.177588	759.0625	3.83601	1024.688
2.300862	780.3125	3.836798	1024.688
2.418926	808.4375	3.837461	1024.688

Table 3. Meniscus location at different time values in an open rectangular channel (d=40 μm).

Time (ms)	Meniscus Location (μm)	Time (ms)	Meniscus Location (μm)
0.012642	9.375	2.249471	1018.125
0.025587	31.875	2.390931	1053.125
0.040799	44.375	2.522557	1080.625
0.070976	79.375	2.667389	1111.875
0.15107	158.125	2.797909	1141.875
0.233998	226.8743	2.93302	1163.125
0.324015	293.125	3.0431	1181.875
0.437987	369.375	3.177139	1203.125
0.529825	420.625	3.298359	1225.625
0.647357	485.625	3.410433	1250.625
0.76966	543.125	3.537451	1269.375
0.892013	604.375	3.646013	1285.625
1.01349	648.1257	3.753629	1301.875
1.1403	694.375	3.873382	1321.875
1.257086	736.875	3.990501	1341.875
1.349495	781.875	4.116654	1359.375
1.477168	810.625	4.243968	1378.125
1.587221	843.125	4.363539	1394.375
1.720567	896.875	4.478563	1416.875
1.851322	921.875	4.604173	1435.625
1.988451	961.875	4.717452	1445.625
2.118741	986.875	4.808013	1458.125

Table 4. Meniscus location at different time values in an open rectangular channel (d=80 µm).

Time (ms)	Meniscus Location (µm)	Time (ms)	Meniscus Location (µm)
0.014636	33.75	1.282416	853.75
0.034728	51.25	1.34778	883.75
0.058386	53.75	1.412847	913.75
0.084286	76.25	1.473781	941.25
0.112116	103.75	1.549623	976.25
0.149692	143.75	1.625799	1008.75
0.190671	178.75	1.687504	1036.25
0.246961	228.75	1.757718	1063.75
0.312807	281.25	1.841193	1113.75
0.375274	328.75	1.915731	1126.25
0.439415	373.75	1.984491	1176.25
0.509065	423.75	2.071319	1188.75
0.582925	471.25	2.149392	1221.25
0.658778	521.25	2.219982	1246.25
0.726368	561.25	2.285828	1266.25
0.79738	601.25	2.353631	1293.75
0.868057	643.75	2.446032	1323.75
0.937193	678.75	2.529121	1353.75
1.004766	713.75	2.627235	1386.25
1.076529	748.75	2.721399	1418.75
1.150052	808.75	2.811274	1443.75
1.214911	821.25	2.902097	1486.25

Table 5. Meniscus location at different time values in an open circular channel (d=10 μm).

Time (ms)	Meniscus Location (μm)	Time (ms)	Meniscus Location (μm)
0.131753	100.9375	6.219459	866.5625
0.30996	170.3125	6.596978	890.9375
0.478785	220.9375	6.964346	915.9375
0.653603	263.4375	7.296292	939.6875
0.845308	304.0625	7.615707	960.3125
1.049846	342.1875	7.991292	983.4375
1.253766	375.9375	8.313562	1004.688
1.45725	406.5625	8.618119	1023.437
1.666139	437.1875	8.910379	1041.563
1.861195	464.6875	9.219176	1058.438
2.083548	492.1875	9.592199	1079.062
2.327806	520.9375	9.941713	1097.813
2.645195	557.1875	10.31792	1119.063
3.025751	595.9375	10.69541	1137.187
3.398486	633.4375	11.0623	1158.437
3.763617	668.4375	11.39604	1175.937
4.123766	700.9375	11.78412	1194.063
4.494923	731.5625	12.14293	1213.438
4.871563	763.4375	12.52509	1232.187
5.200898	790.3125	12.90027	1250.937
5.516032	815.9375	13.26249	1268.437
5.852575	840.3125	13.62686	1286.563

Table 6. Meniscus location at different time values in an open circular channel (d=20 μm).

Time (ms)	Meniscus Location (μm)	Time (ms)	Meniscus Location (μm)
0.045575	57.8125	4.167951	940.3125
0.188924	147.1875	4.432318	972.1875
0.342305	215.9375	4.691428	1000.938
0.507341	276.875	4.944268	1029.063
0.672676	330.9375	5.220644	1057.187
0.808581	374.0625	5.480413	1085.937
0.967388	415.9375	5.737894	1110.937
1.10468	450.9375	5.984643	1136.563
1.231852	480.9375	6.283255	1163.437
1.386913	515.9375	6.562129	1189.688
1.514624	542.8125	6.848347	1214.687
1.680858	575.3125	7.129774	1240.938
1.876832	609.6875	7.431169	1265.937
2.082058	645.9375	7.706209	1293.438
2.288595	680.9375	8.009644	1319.687
2.489183	712.8125	8.316046	1344.375
2.673038	742.1875	8.626095	1368.438
2.856978	770.9375	8.937993	1397.187
3.120736	806.5625	9.20934	1423.437
3.380096	841.5625	9.508173	1444.687
3.646699	875.9375	9.6392	1453.437
3.905722	909.0625	9.653164	1455.312

Table 7. Meniscus location at different time values in an open circular channel (d=40 µm).

Time (ms)	Meniscus Location (µm)	Time (ms)	Meniscus Location (µm)
0.011688	39.375	2.266528	899.375
0.030005	59.375	2.385834	926.875
0.102539	118.75	2.486329	949.375
0.201591	186.875	2.592723	973.125
0.302985	246.875	2.692986	996.875
0.403894	298.75	2.81352	1021.875
0.506298	350.625	2.934156	1045.625
0.613622	393.75	3.031968	1065.625
0.724471	443.125	3.137004	1086.875
0.83024	486.875	3.24069	1108.125
0.942864	522.5	3.346765	1128.125
1.06141	563.75	3.451074	1148.125
1.172332	601.875	3.586103	1174.375
1.278331	633.75	3.754899	1201.875
1.395078	663.75	3.879429	1224.375
1.519178	702.5	3.996532	1244.375
1.627625	736.875	4.16205	1269.375
1.719747	763.125	4.286774	1290.625
1.829112	793.125	4.400957	1310.625
1.955728	823.125	4.504536	1326.875
2.053557	846.875	4.611961	1346.875
2.155907	871.875	4.717417	1364.375

Table 8. Meniscus location at different time values in an open circular channel (d=80 µm).

Time (ms)	Meniscus Location (µm)	Time (ms)	Meniscus Location (µm)
0.00298	6.25	1.439315	811
0.0192	33.7	1.523148	841
0.0418	58.7	1.614328	869
0.0662	93.8	1.709537	904
0.0924	124	1.80125	936
0.135	159	1.884183	964
0.192	204	1.989587	999
0.265	251	2.087959	1033.75
0.356	306	2.181522	1062.5
0.436	351	2.285577	1093.75
0.516	394	2.393025	1127.5
0.584	431	2.486128	1153.75
0.647	464	2.579076	1183.75
0.721	501	2.685619	1216.25
0.812	544	2.797203	1253.75
0.885	576	2.90552	1283.75
0.95	609	2.988549	1306.25
1.024124	639	3.076314	1331.25
1.100704	671	3.15535	1353.75
1.176891	704	3.236025	1376.25
1.259683	736	3.318726	1401.25
1.34934	774	3.403063	1421.25

Table 9. Meniscus location at different time values in a V-shaped channel (d=10 μm, α = 45°).

Time (ms)	Meniscus Location (μm)	Time (ms)	Meniscus Location (μm)
0.33021	146.875	10.34818	784.375
0.787428	236.875	10.78906	801.875
1.249803	298.125	11.24958	819.375
1.713322	346.875	11.69131	834.375
2.171911	389.375	12.14307	849.375
2.637081	424.375	12.6008	861.875
3.09243	461.875	13.04555	876.875
3.548551	489.375	13.49544	894.375
4.001289	519.0625	13.95498	911.875
4.456212	549.0625	14.40583	924.375
4.915178	571.875	14.84622	934.375
5.3782	591.5625	15.29136	945.9375
5.819657	614.375	15.73519	961.875
6.283632	639.375	16.17966	973.4375
6.738927	659.375	16.63117	984.375
7.188067	676.875	17.08369	996.875
7.639176	691.875	17.52681	1005.938
8.092452	709.375	17.97471	1015.938
8.546691	730.9375	18.42514	1024.375
8.99639	744.375	18.87729	1034.375
9.436193	759.375	19.32851	1043.438
9.89363	771.875	19.79192	1054.375

Table 10. Meniscus location at different time values in a V-shaped channel (d=20 μm, α = 45°).

Time (ms)	Meniscus Location (μm)	Time (ms)	Meniscus Location (μm)
0.155051	136.875	9.331394	1291.562
0.433681	255.3125	9.685047	1319.063
0.607968	308.4375	10.29005	1360.937
0.779147	351.5625	10.29605	1361.563
1.003977	397.8125	10.29704	1361.563
1.306757	454.6875	10.29787	1359.688
1.524965	487.1875	10.29956	1360.312
1.734719	519.0625	10.29925	1360.312
1.908817	545.3125	10.30094	1360.312
2.086675	570.9375	10.30063	1360.312
2.327958	607.8125	10.30231	1360.312
2.807981	665.9375	10.30201	1360.312
3.262606	706.875	10.30369	1360.312
3.571131	756.5625	10.30338	1360.312
3.820981	782.1875	10.30507	1360.312
4.055296	812.1875	10.30476	1362.188
4.676097	872.1875	10.30644	1362.188
5.150942	914.0625	10.30614	1360.937
6.371249	999.375	10.30782	1360.937
7.26246	1071.875	10.30751	1360.937
7.73063	1116.875	10.3092	1360.937
8.972249	1261.562	10.30889	1360.937

Table 11. Meniscus location at different time values in a V-shaped channel (d=40 μm, α = 45°).

Time (ms)	Meniscus Location (μm)	Time (ms)	Meniscus Location (μm)
0.00499	25	3.158549	950
0.0147	55	3.353725	966
0.025	71	3.54658	1011
0.037	83	3.730712	1025
0.0681	115	3.931498	1038
0.201	204	4.104702	1086
0.349	270	4.296804	1102
0.502	332	4.484676	1118
0.675	406	4.83356	1174
0.855	462	5.011991	1190
1.039069	526	5.195868	1198
1.209681	575	5.381843	1238
1.364893	606	5.576518	1251
1.538424	642	5.777071	1286
1.70766	703	5.951435	1302
1.889401	726	6.125752	1310
2.069212	758	6.32349	1326
2.244775	803	6.861459	1382
2.441768	822	7.042823	1398
2.635123	878	7.206382	1406
2.814983	894	7.427334	1414
2.979864	910	7.641327	1430

Table 12. Meniscus location at different time values in a V-shaped channel (d=80 μm, α = 45°).

Time (ms)	Meniscus Location (μm)	Time (ms)	Meniscus Location (μm)
0.0148	43.7	1.266161	809
0.0272	63.7	1.348237	836
0.045	93.8	1.436846	874
0.0517	127	1.5196	901
0.0635	119	1.59501	929
0.0875	201	1.682821	956
0.113	231	1.757297	984
0.163	254	1.840123	1011.25
0.228	297	1.91694	1033.75
0.299	347	1.997628	1058.75
0.368	387	2.081133	1083.75
0.437	419	2.15817	1103.75
0.501	464	2.234772	1123.75
0.57	497	2.313134	1148.75
0.647	527	2.398009	1173.75
0.725	567	2.487024	1198.75
0.795	604	2.583085	1226.25
0.87	632	2.678658	1253.75
0.941	674	2.785134	1281.25
1.023482	706	2.879189	1303.75
1.099583	739	2.975177	1333.75
1.1856	779	3.081889	1358.75

Table 13. Meniscus location at different time values in a U-shaped channel (d=10 µm, P=2).

Time (ms)	Meniscus Location (µm)	Time (ms)	Meniscus Location (µm)
0.034361	68.4375	3.55362	988.4375
0.126681	158.75	3.702867	1009.375
0.321773	264.375	3.85151	1034.688
0.511805	341.25	3.996298	1054.063
0.70176	404.375	4.14442	1075.938
0.881132	454.375	4.290933	1097.812
1.050372	501.875	4.44041	1117.188
1.219976	543.125	4.595911	1140.313
1.381798	586.875	4.747496	1160.313
1.543195	619.375	4.889541	1179.688
1.708767	655.9375	5.046106	1200.938
1.881501	690.9375	5.199461	1219.688
2.041932	723.125	5.343897	1238.438
2.216425	755.9375	5.49837	1259.688
2.372678	787.1875	5.657728	1279.063
2.526673	816.5625	5.816023	1296.875
2.673804	844.0625	5.962118	1317.188
2.824112	869.0625	6.117774	1330.938
2.971094	894.6875	6.272545	1354.063
3.115638	919.6875	6.423756	1372.188
3.263226	942.8125	6.569162	1389.688
3.40997	965.9375	6.718203	1408.438

Table 14. Meniscus location at different time values in a U-shaped channel (d=20 μm, P=2).

Time (ms)	Meniscus Location (μm)	Time (ms)	Meniscus Location (μm)
0.00572	22.2	2.11706	1010.313
0.0135	38.1	2.224213	1034.375
0.0351	72.5	2.327519	1057.813
0.11	169	2.431654	1083.125
0.198	252	2.535849	1108.438
0.304	329	2.633928	1130.313
0.414	399	2.737335	1154.688
0.523	454	2.837686	1177.812
0.634	511	2.938757	1199.687
0.745	559	3.042799	1220.937
0.859	609	3.141741	1242.812
0.966	651	3.237587	1260.938
1.076772	691	3.342623	1285.312
1.190336	734	3.445761	1304.687
1.29702	771	3.547648	1325.313
1.407778	804	3.646348	1344.688
1.512977	842	3.751471	1364.687
1.612764	871	3.849046	1383.438
1.717741	897	3.952744	1403.437
1.816541	924	4.055474	1421.563
1.917815	962	4.150337	1440.312
2.016773	988	4.248177	1459.062

Table 15. Meniscus location at different time values in a U-shaped channel (d=40 µm, P=2).

Time (ms)	Meniscus Location (µm)	Time (ms)	Meniscus Location (µm)
0.00548	13.1	0.956	795
0.0117	21.9	1.037886	834
0.016	26.9	1.121594	875
0.02	33.1	1.197281	913
0.0235	36.9	1.274764	958
0.0286	44.4	1.351126	988
0.0338	50.6	1.432536	1025
0.0398	61.3	1.51365	1063.75
0.0499	76.9	1.589881	1092.5
0.0632	93.8	1.661659	1127.5
0.085	123	1.740332	1157.5
0.115	165	1.817553	1185
0.173	231	1.889602	1213.75
0.236	294	1.964974	1252.5
0.303	354	2.04484	1277.5
0.371	413	2.116683	1301.875
0.437	463	2.198642	1327.5
0.511	518	2.280975	1347.5
0.586	569	2.353537	1378.125
0.661	615	2.42622	1408.75
0.729	658	2.502194	1433.75
0.806	708	2.574399	1447.5

Table 16. Meniscus location at different time values in a U-shaped channel (d=80 μm, P=2).

Time (ms)	Meniscus Location (μm)	Time (ms)	Meniscus Location (μm)
0.007742	36.25	0.716163	696.25
0.016821	53.75	0.772714	738.75
0.026925	76.25	0.823158	778.75
0.036463	88.75	0.875696	818.75
0.046902	93.75	0.928914	857.5
0.054046	98.75	0.984489	893.75
0.06426	108.75	1.042336	933.75
0.074088	121.25	1.100349	968.75
0.08668	133.75	1.163122	1008.75
0.106475	153.75	1.22615	1048.75
0.127926	173.75	1.284274	1087.5
0.152026	196.25	1.349003	1123.75
0.175808	218.75	1.409463	1157.5
0.210812	251.25	1.475109	1197.5
0.252507	293.75	1.546297	1237.5
0.297821	338.75	1.612198	1273.75
0.345582	383.75	1.682478	1313.75
0.396026	431.25	1.750472	1347.5
0.449356	476.25	1.821732	1387.5
0.498584	518.75	1.890711	1426.25
0.552492	563.75	1.960989	1462.5
0.610518	608.75	2.024228	1493.75

REFERENCES

[1]   K.-Y. Weng, N.-J. Chou, and J.-W. Cheng, "Triggering vacuum capillaries for pneumatic pumping and metering liquids in point-of-care immunoassays," Lab Chip, vol. 8, no. 7, pp. 1216–1219, 2008.

[2]   C. D. Chin, S. Y. Chin, T. Laksanasopin, and S. K. Sia, "Low-cost microdevices for point-of-care testing," in Point-of-care Diagnostics on a chip, Springer, 2013, pp. 3–21.

[3]   M. Boyd and T. Woolley, "Point of care testing," Surgery-Oxford Int. Ed., vol. 34, no. 2, pp. 91–93, 2016.

[4]   Y.-F. Tsai, C.-J. Shieh, and H. Yang, "Capillary force pumping fluid for glucose oxidase enzymatic fuel cells," Microsyst. Technol., vol. 23, no. 9, pp. 3927–3935, 2017.

[5]   J. P. McHale and S. V Garimella, "Heat transfer in trapezoidal microchannels of various aspect ratios," Int. J. Heat Mass Transf., vol. 53, no. 1–3, pp. 365–375, 2010.

[6]   D. G. Gilmore and M. Bello, Satellite thermal control handbook, vol. 1. Aerospace Corporation Press EI Segundo, CA, 1994.

[7]   W. W. Wits, H. J. Ten Hoeve, G. W. Te Riele, and J. Van Es, "System for fast and accurate filling of a two-phase cooling device, notably a heat pipe, adapted for use in an automated process." Google Patents, 03-Jan-2017.

[8]   J. R. JAEKLE D, "Propellant management device conceptual design and analysis-Vanes," in 27th Joint Propulsion Conference, 1991, p. 2172.

[9]   R. Srinivasan, "Estimating zero- g flow rates in open channels having capillary pumping vanes," Int. J. Numer. methods fluids, vol. 41, no. 4, pp. 389–417, 2003.

[10]   C. Lin and X. Zhang, "A Bio-Wicking System to Mitigate Capillary Water in Base Course," 2016.

[11]   J. N. Israelachvili and H. Wennerstroem, "Entropic forces between amphiphilic surfaces in liquids," J. Phys. Chem., vol. 96, no. 2, pp. 520–531, 1992.

[12]   T. Young, "III. An essay on the cohesion of fluids," Philos. Trans. R. Soc. London, vol. 95, pp. 65–87, 1805.

[13]   P. Bronowicki, P. Canfield, A. Grah, and M. Dreyer, "Free surfaces in open capillary channels-Parallel plates," Phys. Fluids, vol. 27, no. 1, 2015.

[14] F.-C. Li, H. Kinoshita, X.-B. Li, M. Oishi, T. Fujii, and M. Oshima, "Creation of very-low-Reynolds-number chaotic fluid motions in microchannels using viscoelastic surfactant solution," Exp. Therm. Fluid Sci., vol. 34, no. 1, pp. 20–27, 2010.

[15] M. Rudman, "A volume-tracking method for incompressible multifluid flows with large density variations," Int. J. Numer. methods fluids, vol. 28, no. 2, pp. 357–378, 1998.

[16] M. Sussman, E. Fatemi, S. Osher, and P. Smereka, "A level set approach for computing solutions to incompressible two-phase flow II," Lawrence Livermore National Lab., CA (United States), 1995.

[17] V. E. Badalassi, H. D. Ceniceros, and S. Banerjee, "Computation of multiphase systems with phase field models," J. Comput. Phys., vol. 190, no. 2, pp. 371–397, 2003.

[18] J. E. Pilliod Jr and E. G. Puckett, "Second-order accurate volume-of-fluid algorithms for tracking material interfaces," J. Comput. Phys., vol. 199, no. 2, pp. 465–502, 2004.

[19] R. Gupta, D. F. Fletcher, and B. S. Haynes, "On the CFD modelling of Taylor flow in microchannels," Chem. Eng. Sci., vol. 64, no. 12, pp. 2941–2950, 2009.

[20] M. N. Kashid, A. Renken, and L. Kiwi-Minsker, "CFD modelling of liquid–liquid multiphase microstructured reactor: Slug flow generation," Chem. Eng. Res. Des., vol. 88, no. 3, pp. 362–368, 2010.

VITA

Mehrad Gholizadeh Ansari received a bachelor's degree in Chemical Engineering from the School of Engineering, University of Tehran in July 2015. In July 2018, he received his M.S. Degree in Environmental Engineering from Missouri University of Science and Technology. He worked in the geo-technology research group at Missouri S&T as a Graduate Assistant. His research involved numerical modeling of spontaneous capillary-driven flow in open microchannels using the finite volume analysis and high-performance computing.